THE UNIVERSITY *of* EDINBURGH

Edinburgh Research Explorer

Ozone chemistry on tidally locked M dwarf planets

OPEN ACCESS

Ozone chemistry on tidally locked M dwarf planets

Jack S. Yates,[1,2] Paul I. Palmer[1,2]⋆, James Manners[3], Ian Boutle[3], Krisztian Kohary[4], Nathan Mayne[4], Luke Abraham[5,6]

[1] *School of GeoSciences, University of Edinburgh, King's Buildings, Edinburgh, EH9 3FF, UK*
[2] *Centre for Exoplanet Science, University of Edinburgh, Edinburgh, UK*
[3] *Met Office, Exeter, EX1 3PB, UK*
[4] *Astrophysics Group, University of Exeter, Exeter, EX4 2QL, UK*
[5] *National Centre for Atmospheric Science, University of Cambridge, CB2 1EW, UK*
[6] *Department of Chemistry, University of Cambridge, Cambridge, CB2 1EW, UK*

ABSTRACT

We use the Met Office Unified Model to explore the potential of a tidally locked M dwarf planet, nominally Proxima Centauri b irradiated by a quiescent version of its host star, to sustain an atmospheric ozone layer. We assume a slab ocean surface layer, and an Earth-like atmosphere of nitrogen and oxygen with trace amounts of ozone and water vapour. We describe ozone chemistry using the Chapman mechanism and the hydrogen oxide (HO_x, describing the sum of OH and HO_2) catalytic cycle. We find that Proxima Centauri radiates with sufficient UV energy to initialize the Chapman mechanism. The result is a thin but stable ozone layer that peaks at 0.75 parts per million at 25 km. The quasi-stationary distribution of atmospheric ozone is determined by photolysis driven by incoming stellar radiation and by atmospheric transport. Ozone mole fractions are smallest in the lowest 15 km of the atmosphere at the sub-stellar point and largest in the nightside gyres. Above 15 km the ozone distribution is dominated by an equatorial jet stream that circumnavigates the planet. The nightside ozone distribution is dominated by two cyclonic Rossby gyres that result in localized ozone hotspots. On the dayside the atmospheric lifetime is determined by the HO_x catalytic cycle and deposition to the surface, with nightside lifetimes due to chemistry much longer than timescales associated with atmospheric transport. Surface UV values peak at the substellar point with values of 0.01 W/m^2, shielded by the overlying atmospheric ozone layer but more importantly by water vapour clouds.

Key words: planets and satellites: atmospheres – planets and satellites: terrestrial planets – astrobiology

1 INTRODUCTION

We are only just beginning to classify the rapidly growing number of extrasolar planets (exoplanets) that orbit stars outside our solar system. In the absence of other reference points, this classification exercise is guided by the mass and radii of solar system planets, even though they may not share similar evolutionary pathways (Seager et al. 2007; Spiegel et al. 2014; Weiss & Marcy 2014). Exoplanets range from scientific curiosities (e.g. COROT-Exo-7b, Léger, A. et al. 2009) to candidates for supporting life (Quintana et al. 2014; Anglada-Escudé et al. 2016; Gillon et al. 2017). Using ever more sophisticated technology, we are now detecting Earth-like exoplanets that receive similar amounts of stellar irradiation as Earth receives from the Sun, placing them into the circumstellar habitable zone (CHZ). From an anthropocentric perspective, the CHZ is a region around the host star that would support liquid water on the planetary surface, a requirement for life (Kasting 1988; Kasting et al. 1993); meeting this criterion means a planet is habitable and not that it is necessarily inhabited. A zeroth order estimate of the CHZ

⋆ E-mail: pip@ed.ac.uk

can be determined from the stellar irradiance and the star-planet distance. However, planetary atmospheres play a significant role in the planetary energy balance depending on atmospheric composition, e.g. infrared absorbers such as greenhouse gases (Meadows & Barnes 2018) and reflecting and absorbing aerosol particles and clouds. Consideration of a planetary atmosphere is therefore integral for understanding whether an exoplanet is habitable. Here, we use the computational framework from a leading 3-D Earth system model to describe the interplay between atmospheric dynamics and a simplified description of atmospheric ozone chemistry on a tidally-locked M dwarf planet, nominally Proxima Centauri b (Anglada-Escudé et al. 2016). The planet is irradiated by a M dwarf spectrum that is representative of an older, quiescent version of its host star. We use 3-D model calculations to study variations in atmospheric ozone and to understand how ozone affects the habitability of the planet, e.g. surface UV environment and broader impacts on climate.

The first detections of planets around main-sequence stars came in 1995 (Mayor & Queloz 1995). In the 2000s, automated surveys revolutionised the field yielding vast quantities of planet detections (e.g. Borucki (2016)). To date, thousands of exoplanets have been discovered (e.g. Morton et al. 2016; Thompson et al. 2018) across a broad range of bulk planetary properties. Telescope and detector technologies have already allowed characterisation of giant exoplanet atmospheres through transmission (e.g., Sing et al. (2011)) and emission (e.g., Todorov et al. (2014)) spectroscopy and direct imaging (Lagrange et al. 2010). The first detection of an exoplanet atmosphere was achieved using transmission spectroscopy and showed absorption by the sodium doublet in the atmosphere of the hot Jupiter HD 209458b (Charbonneau et al. 2002). Recent surveys have detected Earth-sized planets on close orbits around cold M dwarf stars, notably Proxima Centauri b (Anglada-Escudé et al. 2016) and the TRAPPIST 1 planets (Gillon et al. 2017). For these planets, orbital distance and low stellar flux compensate for each other, resulting in Earth-like levels of top-of-the-atmosphere radiation, placing them in the CHZ (Kasting et al. 1993).

It is no coincidence that these planets have thus far been detected only around M dwarf stars. These stars represent 70% of all stars (Bochanski et al. 2010), and the detectability of their orbiting planets is greater due to the increased planet-to-star radius ratio. The detectability of a planet also increases as the orbital semi-major axis decreases because of the diminished effect of inclination and the subsequent increased frequency of transits and the larger radial-velocity signature. Demographic studies suggest that M dwarfs are more likely than larger stars to host small planets (Shields et al. 2016). Collectively, these observational factors suggest that M dwarfs are our best hope for finding exoplanets in the CHZ. However, there are many unknowns in the habitability assessment of a candidate M dwarf, e.g. the manifold impacts of climate on stellar and planetary environments (Shields et al. 2016). Until telescopes are capable of detailed observations of M dwarf planets, we are limited to examining them through investigative modelling efforts and focus on the influence of atmospheric chemical composition.

Previous studies using general circulation models (GCMs) have shown that close-in M dwarf planets, tidally locked or otherwise, may be habitable (e.g. Boutle et al. 2017; Kopparapu et al. 2017; Turbet et al. 2017; Meadows et al. 2018). For a terrestrial planet the global circulation is driven almost entirely by stellar radiation, which is by far the largest heat source in the system. Naturally this creates spatial inhomogeneities. For a tidally-locked planet with a permanent day and night side, these inhomogeneities are even more exaggerated. In this scenario, the 3-dimensional nature of the system – a hot day side, a cold night side and an atmospheric jet transporting heat and moisture around the equator – means that 1-dimensional models are not necessarily sufficient to properly simulate the atmospheric dynamics. This is especially true when clouds and convection are involved, as these processes are difficult to simulate in 1 dimension (see e.g. Tompkins 2000; Palmer 2012, for a discussion of these difficulties). Historically, GCM studies of M dwarf planets have not incorporated an interactive chemistry scheme, partly due to the uncertainties in the atmospheric composition, partly due to the perceived sufficiency of understanding atmospheric chemistry using 1D models, and partly because of the perception that it plays a insignificant contribution to the mean climate. Informed by the results from GCMs, one might expect that the spatial inhomogeneities in the circulation and dynamics drives non-uniform chemistry, resulting in planets that have different day- and nightside chemical environments (Proedrou & Hocke 2016; Drummond et al. 2018). This is relevant to tidally locked planets, which have: broad Rossby gyres on the night side (Showman & Polvani 2011) that temporarily trap air that is consequently subject to extended periods of radiative cooling, resulting in localized cold spots; extreme day-night temperature differences compared with a fast-rotating planet like Earth; and portions of the atmosphere or surface that are never exposed to stellar radiation.

Integrating atmospheric chemistry and physics into GCMs is therefore a natural next step for exoplanet science, and is relevant also for understanding and testing potential atmospheric biosignatures (Seager 2014). Spatial inhomogeneities in atmospheric biosignatures, driven by atmospheric chemistry and physics, will affect our ability to detect them (e.g. transmission geometry) and to interpret them in the absence of 3-D models. In the case of habitable M-dwarf planets, direct detection, where spectra are hemispherically averaged, is not likely to be possible for many years due to their associated small angular separations from their host star. Transmission and thermal phase curves therefore represent the main current observing modes for these planets, for which terminator profiles and day-night contrasts will be the most important. Conversely, the observed variations in these biosignatures, interpreted using 3-D model analogues, may identify which ones are most robust.

Previous work that studied a tidally locked Earth, although orbiting the Sun in 365 days, showed significant chemical differences on the day and night side of the planet (Proedrou & Hocke 2016). Using a simple ozone photochemistry model, they showed that ozone was present on both sides but was present in higher concentrations on the night side. They also found that for the night side, where chemical e-folding lifetimes are longest, atmospheric transport was most important for

Parameter	Value
Semi-major axis / AU	0.0485
Stellar irradiance / W m^{-2}	881.7 (0.646)
Orbital period / Earth days	11.186
Ω /rad s^{-1}	6.501 $\times 10^{-6}$
Eccentricity	0
Obliquity	0
Radius / km	7160 (1.1)
g / m s^{-1}	10.9

Table 1. Planetary parameters for the simulated Proxima Centauri b planet. Numbers in round brackets represent the ratio with resepect to values for Earth.

determining ozone distributions. This work only has limited applicability to M dwarf planets such as Proxima Centauri b. The stellar radiation spectrum plays a critical role in determining ozone chemistry. It is unclear *a priori* whether a star emitting less UV radiation than the Sun would be able to establish and sustain an ozone layer. Generally, being able to maintain a layer of radiatively active gas, such as ozone, will influence the habitability of the planet directly via the surface radiation environment and indirectly via climate feedbacks. Recent work has used the CAM-Chem 3-D model to study of atmospheric chemistry on M dwarfs (Chen et al. 2018). These authors also discussed the day-night differences in chemistry, and emphasized the importance of using self-consistent chemistry fields for interpreting observations. We discuss this study in the context our work later in section 4.

In this work we examine the sustainability of an ozone layer on a tidally locked M dwarf planet. We use a global 3-D GCM that describes a terrestrial exoplanet, nominally Proxima Centauri b, building on Boutle et al. (2017). The GCM is a generalized version of the Met Office Unified Model (UM), which is used extensively for short-term weather prediction and long-term climate studies for the Earth (Walters et al. 2017). The UM has been used previously to study the atmospheric physics of terrestrial exoplanets and hot Jupiters (e.g. Mayne et al. (2014a,b); Boutle et al. (2017); Lewis et al. (2018); Drummond et al. (2018)). We couple this model with the Chapman mechanism (Chapman 1930) that describes ozone chemistry in Earth's stratosphere with the hydrogen oxide catalytic cycle. The UM and the atmospheric chemistry are described in Section 2. In Section 3, we report our results that describe variations of atmospheric ozone on a tidally-locked M dwarf planet and the responsible chemical reactions. We conclude the paper in Section 4.

2 MODEL DESCRIPTION

Table 1 shows an overview of the physical parameters that define the Proxima Centauri b simulation, following Boutle et al. (2017). For the sake of brevity, we focus here on key aspects of the simulation and refer the reader to Mayne et al. (2014a,b); Boutle et al. (2017) for a comprehensive model description. We run the model at a horizontal spatial resolution of 2° (latitude) ×2.5° (longitude), with the substellar point defined at latitude and longitude 0°. We increase the upper altitude boundary of the model from 40 km (Boutle et al. 2017) to 85 km, described on 60 levels of which 38 levels describe the atmosphere from the surface to 40 km and are identical to those used by Boutle et al. (2017). We increased the model upper boundary to improve the description of ozone dynamics in the upper atmosphere. We also reduced the dynamical model time step from 20 minutes, as adopted by (Boutle et al. 2017), to 12 minutes to avoid high wind speeds above altitudes of 40 km violating the Courant-Friedrichs-Lewy condition. Chemistry and radiation timesteps were left unchanged from a default value of one hour.

Figure 1 shows our assumed radiation spectrum for Proxima Centauri, taken from BT-Settl model library for an M dwarf with T_{eff} = 3000 K, g = 1000 ms^{-2} and metallicity = 0.3 dex (Rajpurohit et al. 2013). Using this spectrum, which approximately follows a blackbody distribution, allows us to directly compare our results with previous results that used fixed atmospheric composition (Boutle et al. 2017). Consequently, Proxima Centauri emits less radiation at UV wavelengths relevant to the Chapman mechanism (see photochemical reaction 2 below) than the Sun because of its lower blackbody temperature. We acknowledge that this energy distribution does not include stellar activity, so represents a quiescent star, and does not include Lyman-α emission. Numerical experiments by the authors (not shown) suggest that including Lyman-α emissions would likely result in only a small increase in total O$_3$ columns and a small corresponding change in atmospheric heating.

The UM has the capability to describe gas (Morgenstern et al. 2013; Telford et al. 2013) and aerosol phase (Mann et al. 2010) chemical mechanisms, developed collectively under the UK Chemical and Aerosol (UKCA) project, that is typically used to explore how atmospheric composition affects Earth's climate. Here, we use relatively simple ozone chemistry (described below), but the underlying infrastructure allows this work to be easily extended to study more complex organic chemistry. The atmospheric chemistry is fully 3-D with advection and turbulent mixing, and chemical species are included in the radiation scheme, making the model self-consistent.

We use the Chapman mechanism (reactions R1–R4, Chapman (1930)) to describe the main characteristics of atmospheric ozone on our tidally-locked M dwarf. This mechanism forms the basis of our understanding of observed variations in
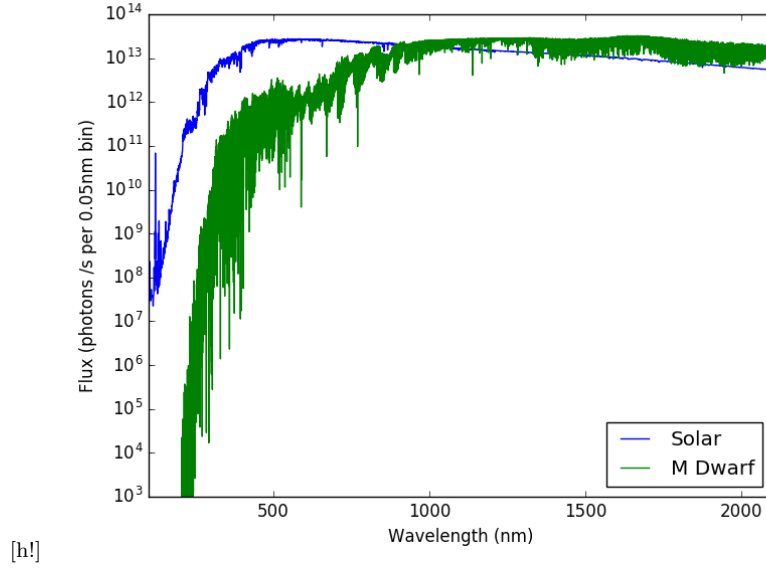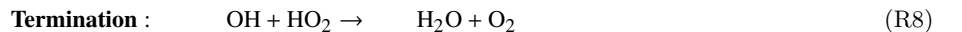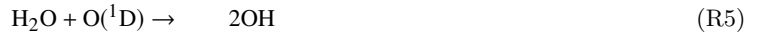
Figure 1. Top-of-the-atmosphere fluxes (photons/s/0.05 nm bin) as a function of wavelength (nm) for Proxima Centauri b (green) and Earth (blue), both scaled to the semi-major axis of orbit.

stratospheric ozone. However, the mechanism overpredicts stratospheric ozone on Earth mainly because it does not take into account catalytic cycles. The mechanism is initiated in R1 by the photolysis of molecular oxygen by high-energy UV photons ($\lambda < 240$ nm), producing atomic oxygen in the ground-level triplet state $O(^3P)$, denoted here as O, which are highly reactive and combine rapidly with O_2 to form ozone (R2). H denotes an inert molecule such as N_2 or O_2 that dissipates the energy associated with the reaction. The resulting ozone molecules can be photolyzed (R3) at longer wavelengths (less energetic photons, $\lambda < 320$ nm) to produce O in its excited singlet state $O(^1D)$ that is rapidly stabilized to $O(^3P)$ by collision with N_2 or O_2. R4 describe the slow loss of ozone due to reaction with atomic oxygen.

$$O_2 + h\nu \rightarrow \quad O + O \quad (\lambda < 240\text{nm}) \tag{R1}$$

$$O + O_2 + H \rightarrow \quad O_3 + H \tag{R2}$$

$$O_3 + h\nu \rightarrow \quad O_2 + O \quad (\lambda < 320\text{nm}) \tag{R3}$$

$$O_3 + O \rightarrow \quad O_2 + O_2 \tag{R4}$$

We include the HO_x (sum of the hydroxyl radical OH and hydroperoxy radical HO_2) catalytic cycle (Roney 1965), acknowledging that our atmosphere also includes water vapour that can lead to ozone loss.

$$H_2O + O(^1D) \rightarrow \quad 2OH \tag{R5}$$

$$OH + O_3 \rightarrow \quad HO_2 + O_2 \tag{R6}$$

$$HO_2 + O_3 \rightarrow \quad OH + 2O_2 \tag{R7}$$

$$\textbf{Termination}: \quad OH + HO_2 \rightarrow \quad H_2O + O_2 \tag{R8}$$

The catalytic cycle comprises of an initiation step (R5), propagation steps that destroy ozone and recycle the catalysis (R6 and R7), and a termination step that represents a loss of the catalysis (R8). We also retain values used by UKCA for ozone dry deposition, which represents a minor loss terms except near the planetary surface. We describe dry deposition of ozone over water following Giannakopoulos et al. (1999), using a value of 0.05 cm s^{-1} (Ganzeveld & Lelieveld 1995).

We define our initial conditions using an Earth-like configuration, comprised of N_2 (approximately 77%), 23.14% O_2 (mass mixing ratio, MMR) and 0.0594% CO_2 (MMR), with the remainder being composed of ozone chemistry tracers that we describe above. We do not consider CH_4 and N_2O in our atmosphere because these trace gases imply life and significantly complicate our chemical mechanism, but they are included in Boutle et al. (2017). With the exception of N_2, CO_2, O_2 and H_2O, we set the other gases associated with chemistry to a uniformly distributed MMR value of 10^{-9} to minimize the influence of initial conditions on subsequent model fields; H_2O is calculated based on evaporation from the slab ocean. We spin-up the model fields for 20 years from those initial conditions. We find that the atmospheric ozone state reaches a quasi equilibrium after 5–10 years subject to stochastic changes in atmospheric dynamics. As a conservative approach, the results we present here are a mean of 120 days that immediately follow the 20-year spin-up period. We perform three model runs: a calculation

Wavelength band (nm)	TOA flux at 1 AU (photons s^{-1} cm^{-2})
187	2.213
191	2.874
193	3.589
196	1.205×10^1
202	3.502×10^1
208	5.388×10^2
211	6.885×10^2
214	1.684×10^5
261	2.107×10^7
267	4.660×10^7
277	1.922×10^8
295	9.886×10^8
303	1.066×10^9
310	3.349×10^9
316	1.390×10^{10}
333	1.110×10^{11}
380	1.980×10^{12}
574	1.319×10^{15}

Table 2. M dwarf TOA fluxes at spectral bands used by the UKCA model, reported at 1 AU.

including the Chapman O_3 mechanism with and without the HO_x catalytic cycle, and a model run using a fixed Earth-like O_3 distribution, following Boutle et al. (2017).

We use two separate but consistent radiation schemes in the model. The SOCRATES radiative transfer model describes the radiation processes in the physical model using six short-wave and nine long-wave bands (Edwards & Slingo 1996; Manners et al. 2015), and represents the default UM radiation scheme. The chemistry module uses a separate radiation scheme, Fast-JX (Wild et al. 2000; Telford et al. 2013), that is spectrally resolved into 18 bands (Table 2) corresponding to atmospheric chemistry.

3   RESULTS

Here, we report results from our numerical experiments that follow our 20-year spin-up period, as described above. Reported values represent a 120-day mean. We focus our attention on ozone chemistry from our control run, referring the reader to Boutle et al. (2017) for a detailed discussion on the corresponding atmospheric physics and climate. Sensitivity runs will be discussed explicitly with reference to the control run.

3.1   Hemispheric Mean 1-D Meteorological and Ozone Structure

Figure 2 summarizes the physical and chemical systems associated with our control run that includes the reactive ozone chemistry, described by reactions R1–R8. Below an altitude of ten kilometres there are a number of differences between the day and night sides of the tidally locked planet, as expected. Compared to the night side, the day side wind speeds are $\simeq$20 m/s slower, specific humidity is much higher and increases towards the surface, UV is non-zero and falls off steadily as a function of depth associated with cloud cover and ozone chemistry. The small, non-zero amount of humidity on the nightside reflects transport from the dayside near the terminator. Temperature is approximately constant from an altitude of 2 km towards the surface on the day side, while there is a strong negative gradient on the night side over the same altitude range. Above 10 km, there is little difference between the distribution and values of air temperature and wind speed, suggesting an efficient transport of heat between the hemispheres (Yang & Abbot 2014; Lewis et al. 2018). There is a strong peak in wind speed between 20 and 30 km, reflecting a jet stream structure. This is in broad agreement with Boutle et al. (2017).

Figure 2 also shows that ozone is vertically distributed, peaking between 20 and 30 km; this is similar to the structure we find in Earth's atmosphere. This peak in ozone is slightly broader on the nightside, reflecting the presence of cold traps that result in a local build-up of ozone. R1 and R4 describe the production and loss of ozone. On the dayside there is a large production rate due to the photolysis of O_2 throughout the atmosphere, falling off towards the surface due to clouds; this reflects the penetration of UV through the atmosphere. The production rate is much smaller for the nightside, with non-zero values due to transport from the dayside. The dayside loss rate (R4) is highest above 10 km, some 90% smaller than the production rate. The corresponding nightside loss rate is much smaller, mainly due to the absence of $O(^1D)$ produced by the photolysis of O_3. Below 10 km, the dominant loss rates are due to the HO_x catalytic cycle, with a vertical distribution following the abundance of atmospheric humidity, as expected. On the nightside, HO_x radicals are exclusively transported from the dayside, where the associated *in situ* initiation step R5 and the termination step R8 are extremely small (Figure 2).
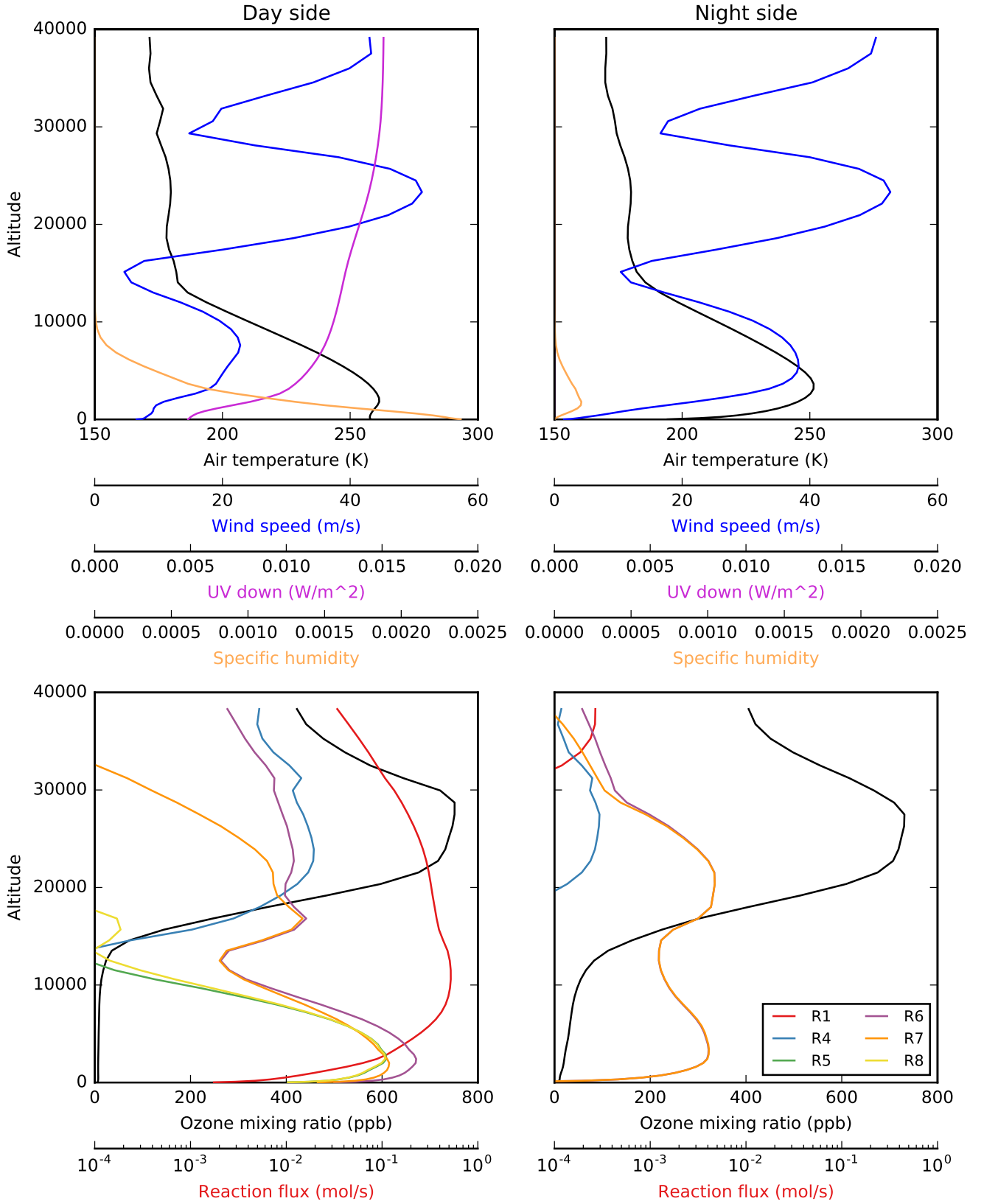
Figure 2. (Left panels) Dayside and (Right panel) nightside hemispheric means of (Top panels) meteorological and (Bottom panels) chemical parameters on a tidally-locked M dwarf planet. Values correspond to a 120-day mean immediately succeeding a 20-year spin-up period. Black lines in the bottom panels show ozone concentration (ppb) per model grid box and the coloured lines show the corresponding reaction fluxes (mol/s), which are plotted on a logarithmic scale as flux per model grid box.
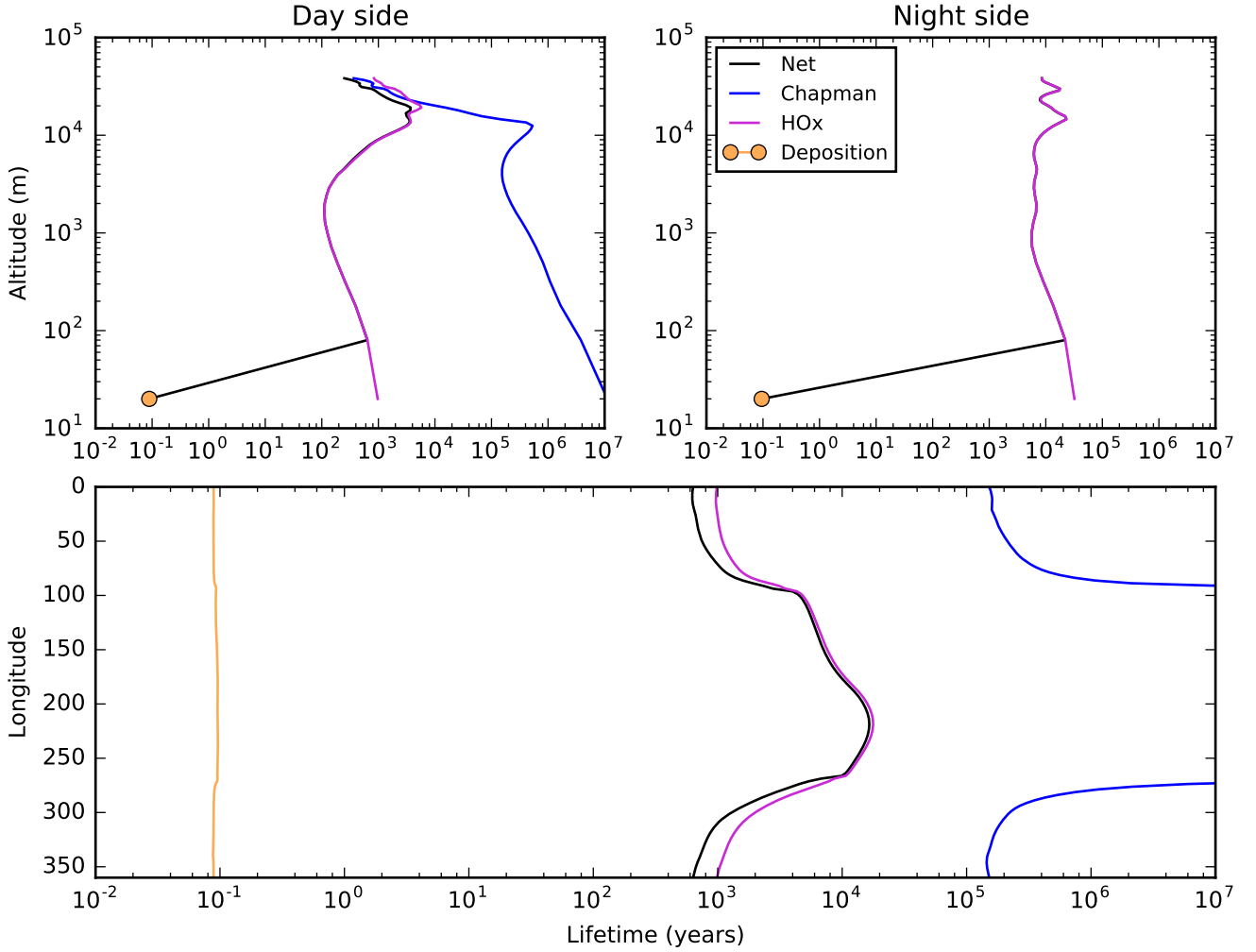
Figure 3. The total and contributing atmospheric lifetimes on a tidally locked M dwarf planet, expressed in years, of atmospheric ozone against chemistry and deposition on the (left panel) dayside and (right panel) nightside hemispheres. The bottom panel describes atmospheric lifetime as a function of longitude (mean taken over latitude and altitude) encompassing both hemispheres. The contributing lifetimes denoted as Chapman and HOx denote the lifetime of ozone against R4 and against the HOx catalytic cycle, respectively. Values correspond to a 120-day mean immediately succeeding a 20-year spin-up period.

Figure 3 shows the lifetime of atmospheric ozone against the Chapman loss term, the HO_x catalytic cycle, and from deposition. We also show the mean net ozone lifetime corresponding to the action of these three loss processes. This lifetime is of the order of hundreds of years, increasing to 10,000 years when ozone is trapped in the nightside cold traps, described below, with a sharp increase in ozone lifetime at the terminators that reflects a rapid decrease in UV radiation necessary to generate atomic oxygen (R1). We find that the loss due to the HO_x catalytic cycle largely determines the net atmospheric lifetime of ozone on the day and nightsides of the planet. The only exception is near the surface where the deposition loss process dominates. The atmospheric lifetime of ozone is an order of magnitude longer on the nightside of the planet, as expected, due to the absence of photons. Atmospheric transport and diffusion processes are orders of magnitude faster than loss processes due to chemistry. The corresponding residence times (non-chemistry lifetimes) typically range 0.1–10 hours in a grid box, and occasionally 100 hours in the laminae layers of low-wind speed that lie between the jet streams, as discussed below.

3.2 3-D Ozone Structure

Here, we focus on the 3-D structure of atmospheric ozone and its precursors, and refer the reader to Appendix A for the associated meteorological fields.

Figure 4 shows the 3-D distribution of atmospheric ozone. We also show integrated column amounts of ozone, expressed in Dobson units (DU) that are commonly used to report ozone in Earth's atmosphere. One DU is defined as the thickness (in

units of 10 microns) of the layer of a pure gas that would be formed by the integrated column amount at standard temperature and pressure, equivalent to 2.69×10^{20} molec/cm^2. Ozone columns are largest on the nightside, localized within two Rossby gyres either side of an approximately uniform equatorial band that corresponds to the rapid transport of air in the equatorial zonal jet (Showman & Polvani 2011). The cyclonic gyres effectively trap air that subsequently experience extended periods of radiative cooling, resulting in localized columns of cold air. Within these cold traps the atmosphere partially collapses (Figure 4, longitude 225°) so that large values of ozone, typical of the higher atmosphere, are brought down to lower altitudes, resulting in higher ozone columns. On the dayside, ozone columns are largest at the poles. The smallest ozone columns ($\simeq$30 DU) are found the dayside at northern and southern midlatitudes. Column ozone values on our M dwarf planet are typically an order of magnitude smaller than those found on Earth ($\simeq$300 DU) with the exception of the interior of the nightside Rossby gyres, where ozone is 140 DU.

Figure 4 also shows atmospheric mole fractions of ozone are at a minimum on the day side near the substellar point. This corresponds to the location of the maximum ozone production and loss rates (R1 and R4), Figures 5 and 6), driven by the availability of incoming UV radiation. The fast exchange between O and ozone, R2 and R3 (Figures 7 and 8, respectively), results in reaction fluxes that are up to five orders of magnitudes larger than that the Chapman production (R1) and loss (R4) fluxes of ozone and peaking on the dayside. In the absence of UV radiation, nightside ozone mole fractions are determined mostly by atmospheric transport but also by the comparatively slow HO_x catalytic cycle loss process. We find that e-folding chemical lifetimes of ozone (Figure B3) within any grid box are much longer than the residence time for an air mass to pass through the same grid box (Figure B4). Initiation of the HO_x catalytic cycle (R5) happens only on the day side, where warmer atmospheric temperatures permit atmospheric humidity, but the propagation reactions R6 and R7 (Figures B1 and B2) continue on the nightside.

To understand the impact of our assumed ozone chemistry mechanism on the climate of Proxima Centauri b, we present model results from a sensitivity run that uses an alternative fixed distribution of Earth-like (larger) ozone that ranges from 2.4×10^{-8} to 1.6×10^{-5} MMR with the largest values in the stratosphere (Boutle et al. 2017). We denote this run as "No chem". We also consider a model run ("No HOx") in which we remove the HO_x ozone catalytic cycle (reactions R5–R8). Figure 9 shows the mean hemispheric dayside and nightside values of the sensitivity minus control runs. On the dayside, "No-chem" ozone results in 5 K warmer and 5 K cooler temperatures above and below 15 km, respectively. Increased temperatures correspond to the altitude of peak ozone due to ozone absorption and heating. On a hemispheric scale, atmospheric ozone reduces the amount of incoming radiation penetrating through the atmosphere, with the largest reductions at the sub-stellar point, thereby cooling altitudes below. Larger Earth-like ozone values result in a near-surface cooling of 2.6 K. We find a similar situation on the nightside, except that near-surface temperatures are 4 K warmer, due to faster movement of dayside polar air to midlatitudes on the nightside. These warmer nightside temperatures are accompanied by higher levels of specific humidity below 10 km. Removing the HO_x catalytic cycle from the interactive chemistry scheme generally has a smaller impact on atmospheric physics than adopting a fixed Earth-like ozone distribution. The catalytic cycle is most important in the upper atmosphere of the sub-stellar point. Figure 9 also show dayside surface UV zonal and meridional mean distributions, which directly reflect the differences between the control and sensitivity ozone distributions.

4 DISCUSSION AND CONCLUDING REMARKS

We use the Met Office Unified Model (UM) to explore the potential of a tidally locked M dwarf planet, nominally Proxima Centauri b irradiated by a quiescent version of its host star, to sustain an atmospheric ozone layer. We have built on previous work (Boutle et al. 2017) by including the Chapman ozone photochemistry mechanism. We have also included the hydrogen oxide (HO_x, describing the sum of OH and HO_2) catalytic cycle to account for atmospheric water vapour that plays a role in determining the distribution of atmospheric ozone. We find that the host M dwarf star radiates with sufficient energy at UV wavelengths to initiate and sustain an ozone layer on Proxima Centauri b. The quasi stationary atmospheric distribution of atmospheric ozone is determined by photolysis driven by incoming stellar radiation and by atmospheric transport. Ozone production rates, determined by the photolysis of molecular oxygen, and loss rates, determined by reaction between ozone and excited atomic oxygen, are largest near the sub-stellar point, as expected. Reaction fluxes involving photolysis get progressively smaller towards the terminators, as expected. Concurrently, excited atomic oxygen is quenched by molecular oxygen to rapidly form ozone, resulting in large ozone concentrations on the nightside of the planet. We find the ozone mole fractions are smallest (largest) in the lowest 15 km of the atmosphere at the (anti) sub-stellar point. Above 15 km the ozone distribution is dominated by an equatorial jet stream that rapidly moves ozone around the planet. The nightside ozone distribution is dominated by two Rossby gyres that leads to prolonged radiative cooling of trapped air, resulting in a localized collapse of the atmosphere that brings down higher ozone values to the lower atmosphere.

The calculations we report here are valid for a quiescent version of the host star. Preliminary calculations (not shown) that crudely describe a stellar electromagnetic flare as a large (150%–600%) and short (1 hr–1 day) perturbation to the quiescent stellar flux received at the top of our unmagnetized planetary atmosphere (Figure 1) show that the ozone layer is resilient. The
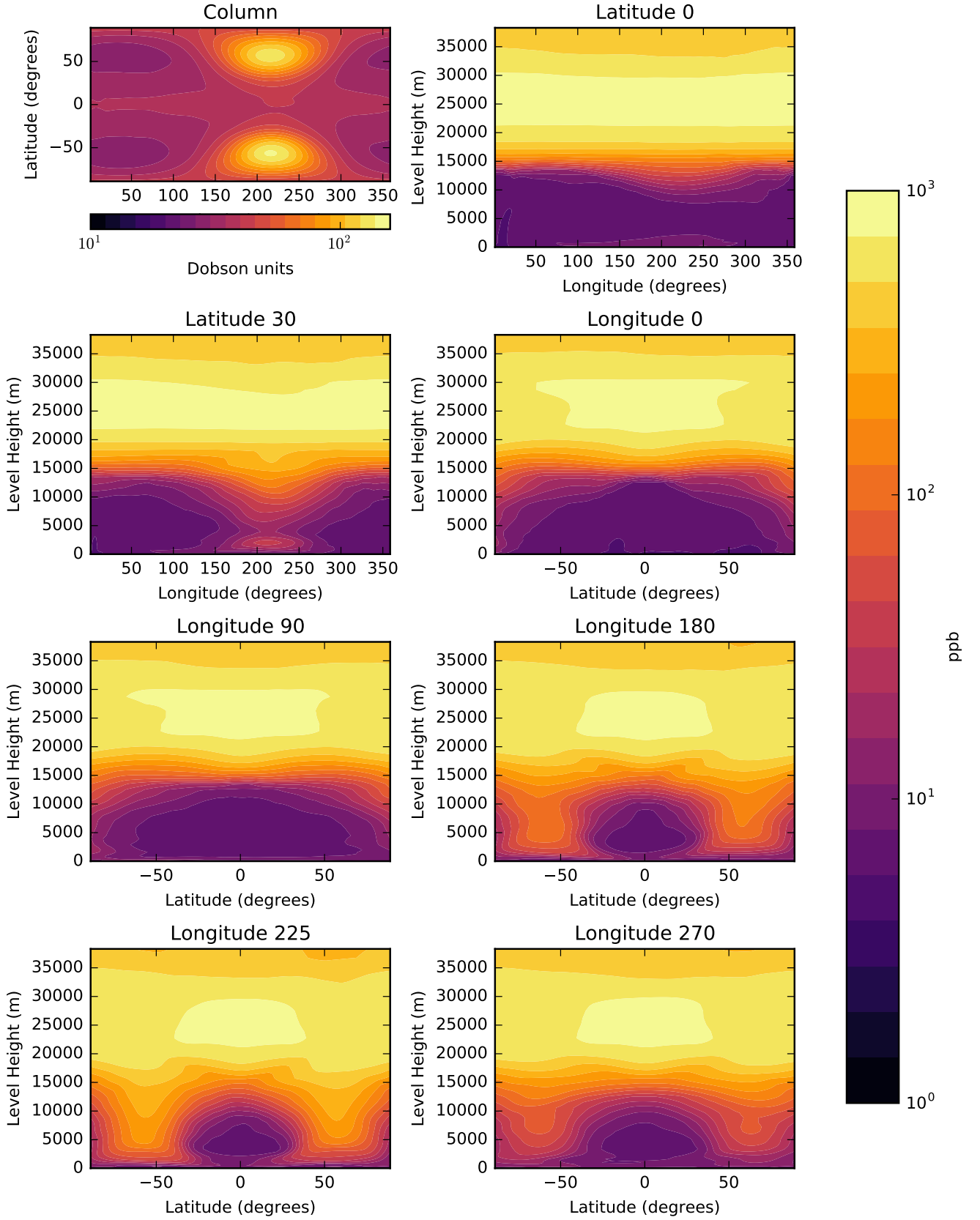
Figure 4. Atmospheric ozone distributions on a tidally-locked M dwarf planet. Values correspond to a 120-day mean immediately succeeding a 20-year spin-up period. The top left panel shows O_3 columns in Dobson units (DU), where one DU is equivalent to a layer of ozone that is 0.01 mm thick at standard temperature and pressure. The remaining panels show meridional or zonal slices that correspond to latitudes and longitudes, respectively, across the planet.
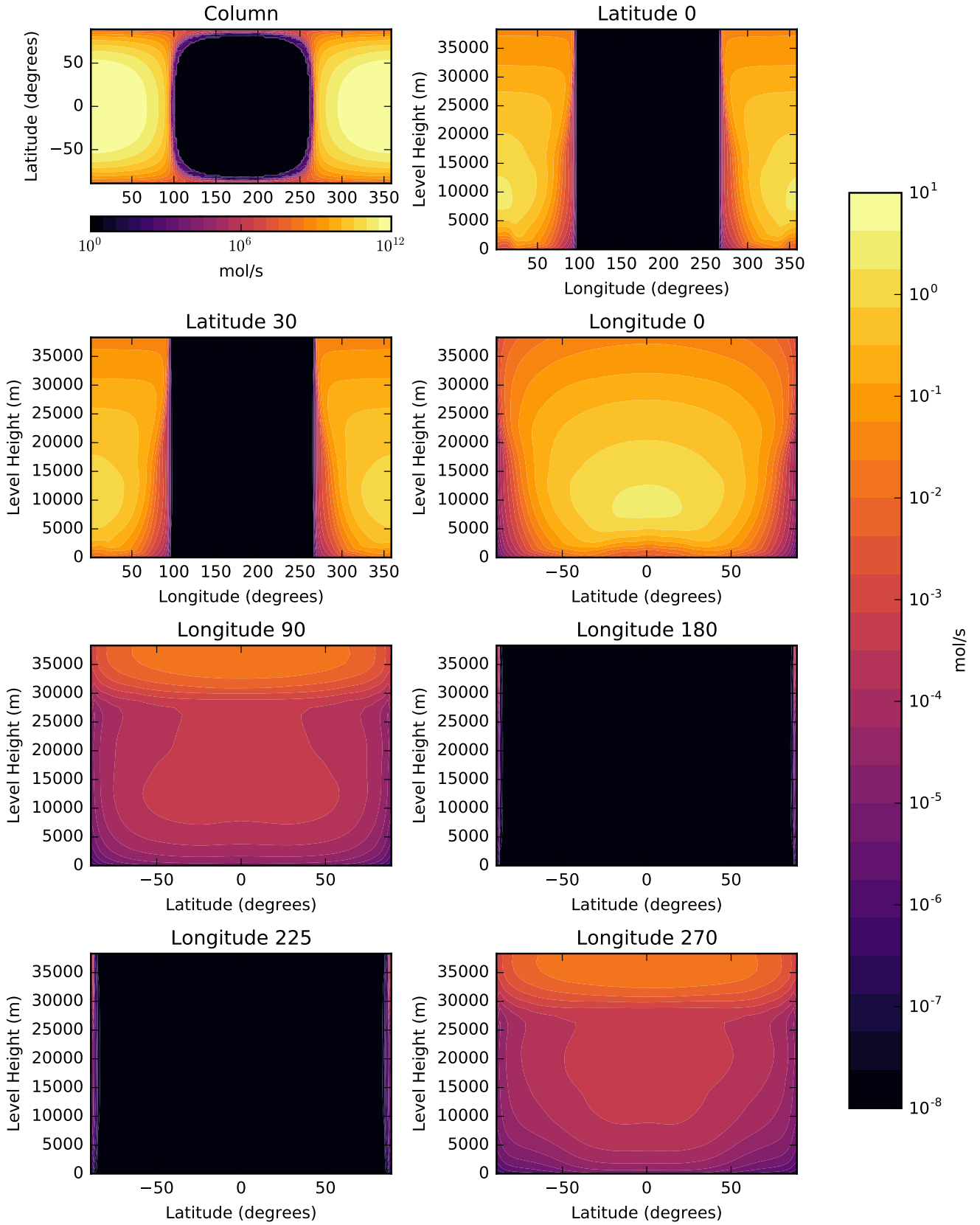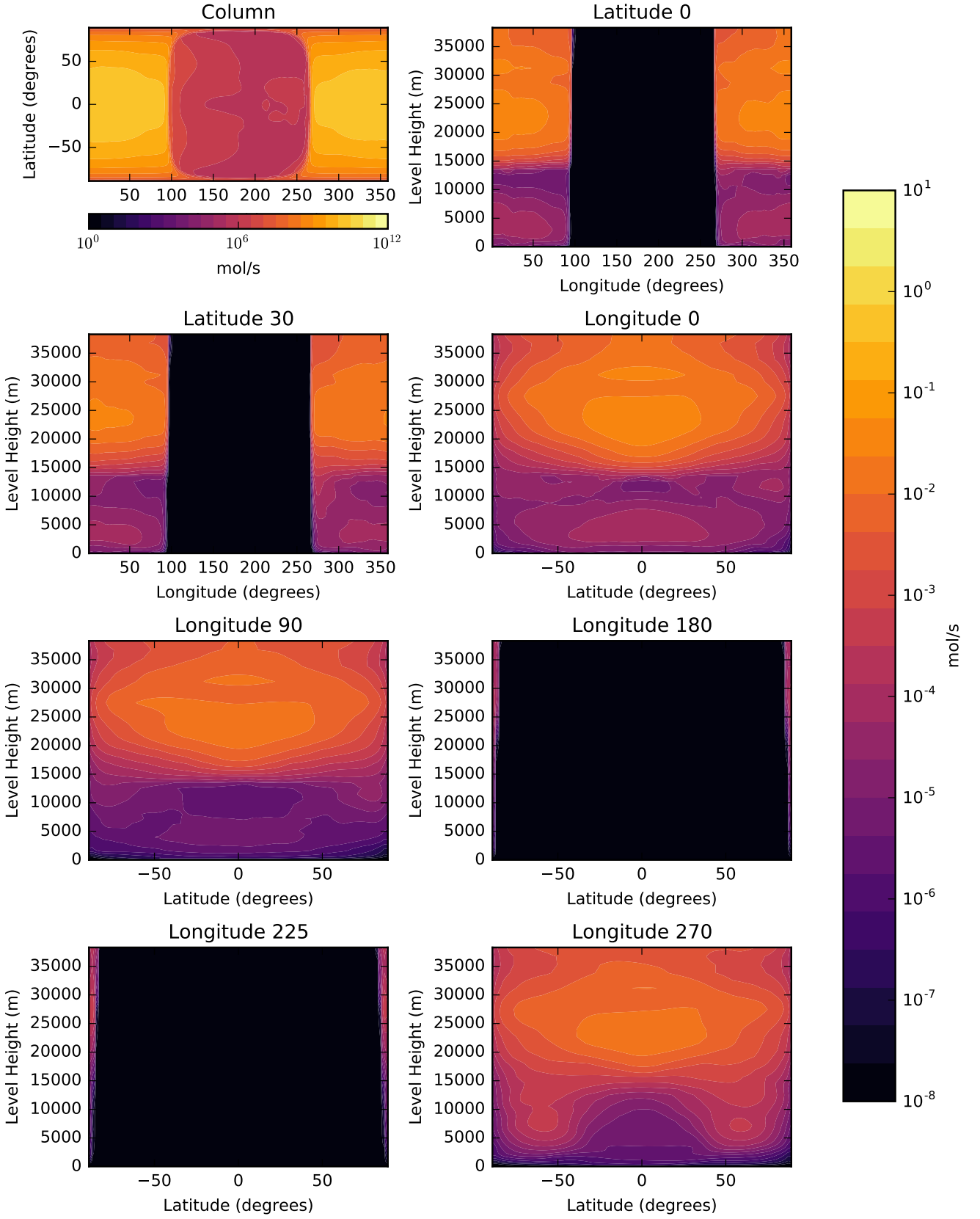
Figure 5. Reaction flux (mol/s) $O_2 + h\nu \rightarrow O + O$ (reaction R1) corresponding to atmospheric ozone distributions on a tidally-locked M dwarf planet. Values correspond to a 120-day mean immediately succeeding a 20-year spin-up period. The format of the plot corresponds to Figure 4.

Figure 6. As Figure 5 but for reaction flux (mol/s) $O_3 + O \rightarrow 2O_2$ (reaction R4).
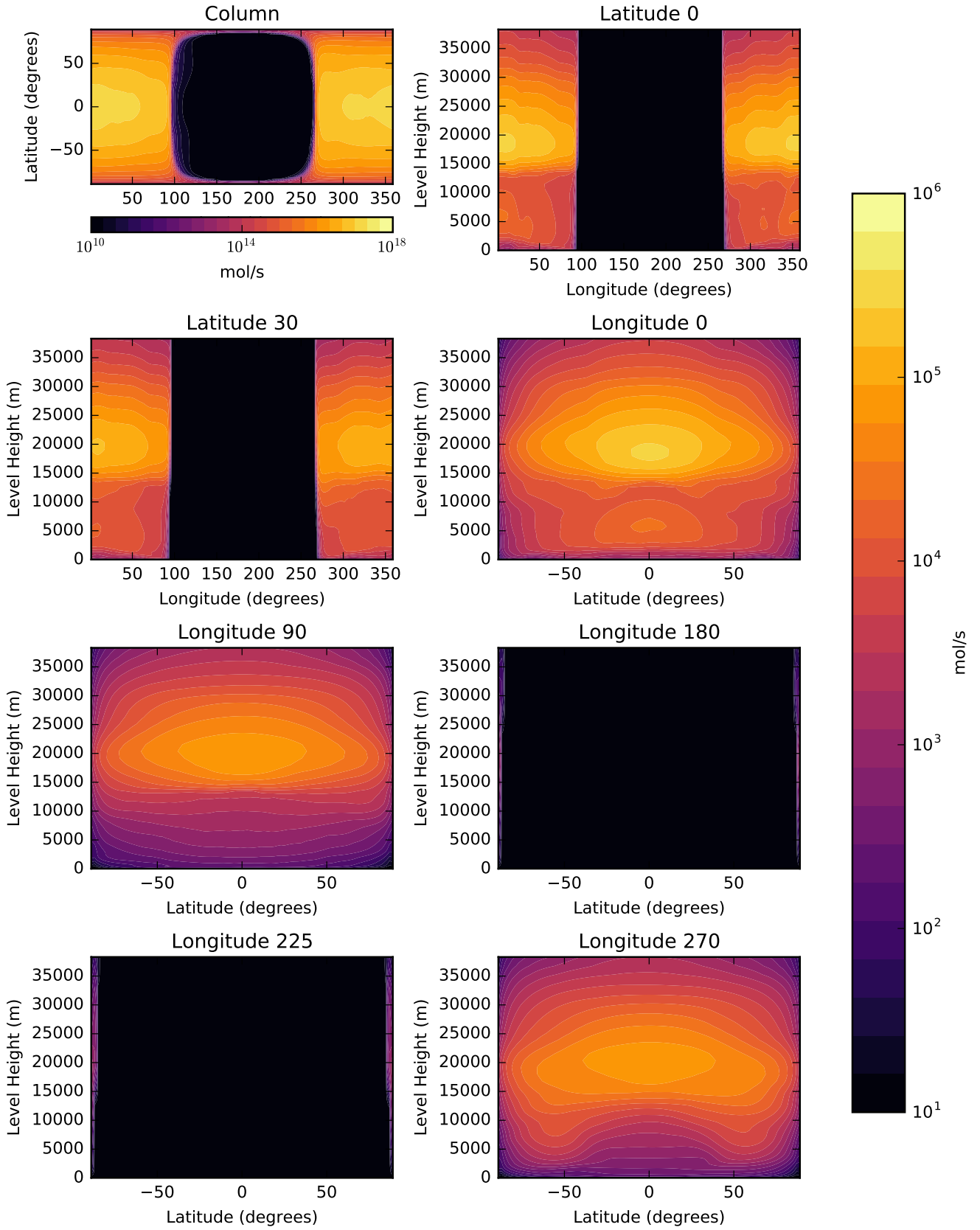
Figure 7. As Figure 5 but for reaction flux (mol/s) $O + O_2 + H \rightarrow O_3 + H$ (reaction R2).
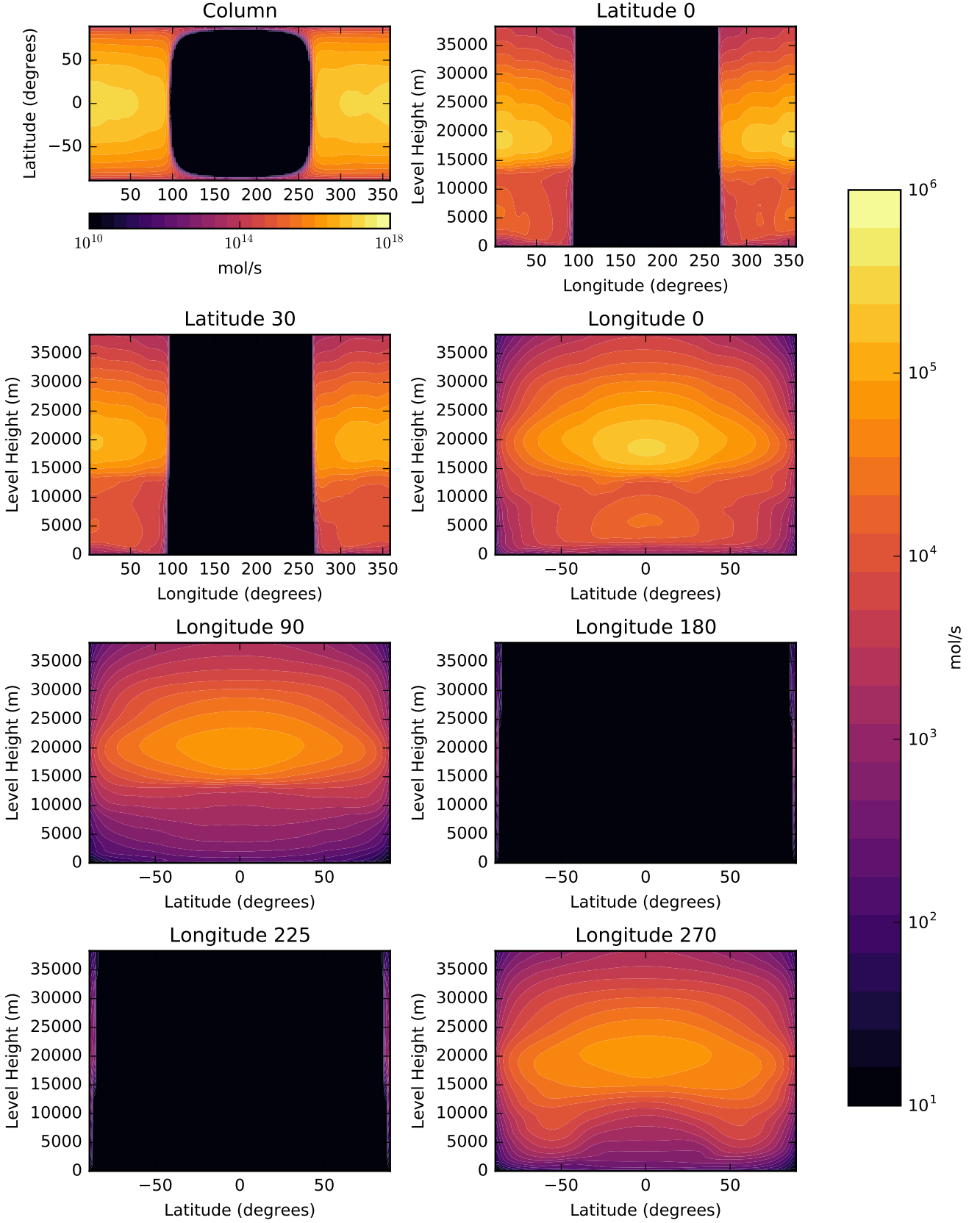
Figure 8. As Figure 5 but for reaction flux (mol/s) $O_3 + h\nu \rightarrow O_2 + O$ (reaction R3).
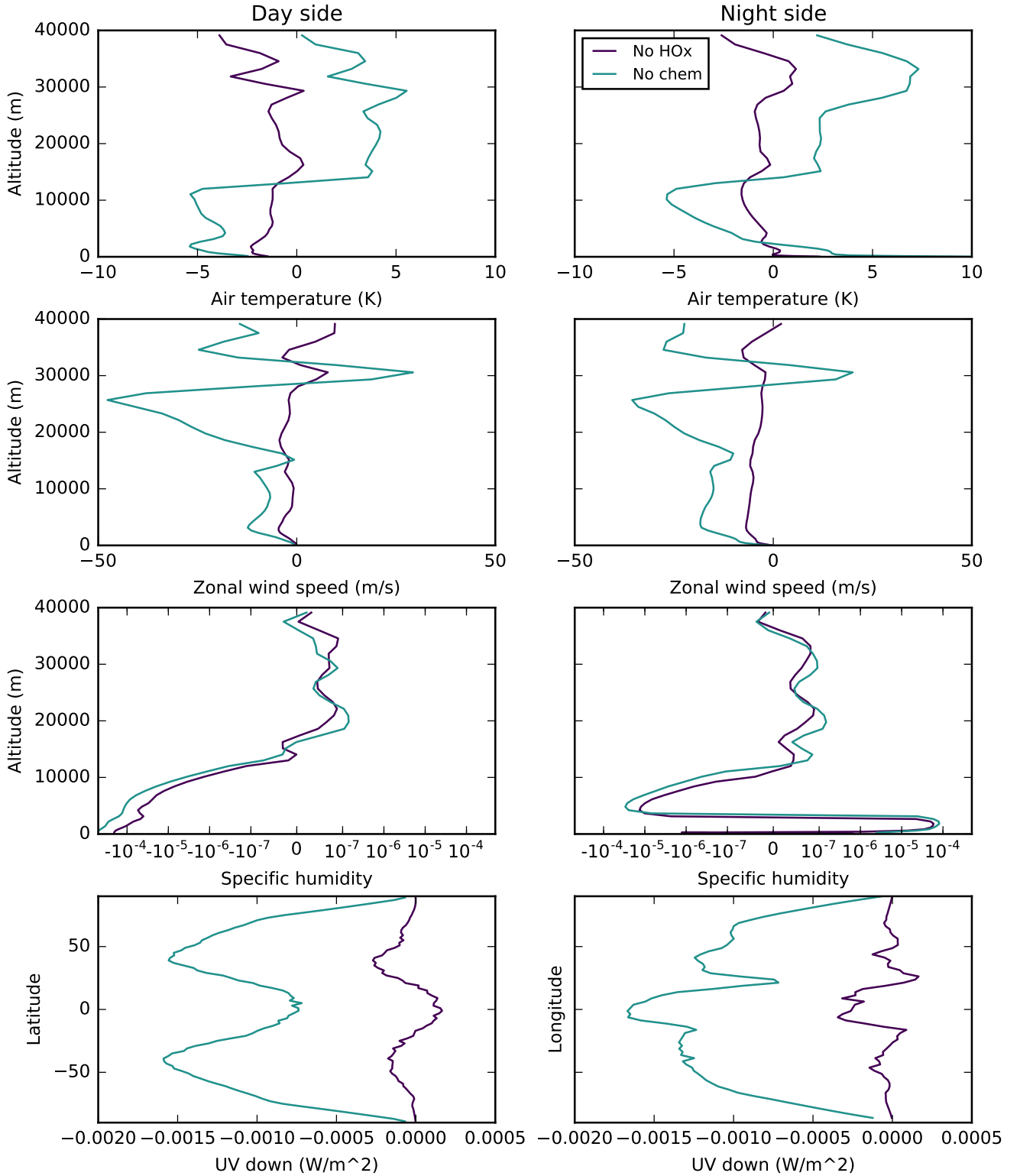
Figure 9. Sensitivity minus control differences of key meteorological parameters on a tidally-locked M dwarf planet that includes atmospheric ozone chemistry. The control calculation describes interactive ozone chemistry, described by the Chapman mechanism and the HO_x catalytic cycle, that is consistent with the physical environment. The two sensitivity runs are 1) No-Chem, which uses a static Earth-like 3-D ozone distribution; and 2) No HO_x, which describes the interactive ozone chemistry but without the catalytic cycle. The top three panels describe (left) dayside and (right) nightside hemispheric mean values. For the specific humidity plot, the abscissa is symmetric about zero: linear between -10^{-7} and 10^{-7}) with the remainder described on a logarithmic scale. The bottom panels show zonal and meridional mean surface UV for the planet dayside.

larger flux of high-energy photons on the dayside titrates O_2 (R1) and low-energy photons titrate O_3 (R3) but can regenerate using products from elevated photolysis fluxes and from reactions active on the nightside. This is qualitatively consistent with 1-D calculations (Segura et al. 2010). More recent 1-D calculations Tilley et al. (2019) report that that if an electromagnetic flare is accompanied by a proton ionization event, ozone can be permanently removed from the atmosphere. The extent of this ozone removal is driven by the magnitude, frequency, and duration of the stellar activity.

We find the planetary surface is potentially habitable in our calculations, in agreement with Boutle et al. (2017), with a significant surface area with temperatures above 273 K. We did not consider ice-albedo feedback, following Shields et al. (2013); Boutle et al. (2017); Lewis et al. (2018) who showed this effect is small for M dwarf planets. For our planetary calculations we adopted Earth-like CO_2 concentrations, but we acknowlege they are likely too low if there exists a carbonate-silicate negative feedback cycle (Walker et al. 1981). This feedback mechanism has the potential to increase the geographical region with surface temperatures above 273 K, depending on a number of factors, e.g. surface geology and tectonic activity.

We show that the thin ozone layer (tens of Dobson units) on the dayside, supported by incoming UV radiation, is sufficient to reduce the incoming UV by 60% from 40 to 0 km, as inferred by reduced photolytic production rates of excited atomic oxygen as a function of atmospheric depth. Previous studies that used a 1-D model found similar results (e.g., O'Malley-James & Kaltenegger 2017). Near-surface warming results in water cloud formation that further reduces the UV penetration in the atmosphere. Surface ozone levels are typically lower than 9 ppb, far below values that are associated with values that trigger human respiratory illnesses and crop damage.

A previous study (Chen et al. 2018) that comes the closest to our experiments is sufficiently different to permit only a qualitative comparison. That study uses the CAM-Chem 3-D model for Earth with an atmospheric chemistry scheme described by 97 species and 196 reactions, in comparison with our model with a reduced description of ozone chemistry. The CAM-Chem model describes atmospheric dynamics using 26 levels (surface–50 km) while our model uses 60 levels (surface–80 km), allowing us to explore in more detail the general circulation. They used stellar insolation of 1360 W m^{-2} while we used 881.7 W m^2, and our stellar spectrum contained less UV radiation that even their quiescent M-dwarf. Finally, (Chen et al. 2018) used Earth continents as part of their surface boundary conditions including a prescribe land/ice scheme, while we use a shallow water world without continents or prescribed ice. Lewis et al. (2018) showed that continents can significantly affect the climate of tidally-locked planets via convection and evaporation of water, but acknowledge that Chen et al. (2018) placed their substellar point in the middle of the Pacific Ocean where there are no large land masses. Despite these many differences between the two experiments, our findings are broadly similar. In particular, the contrast between ozone on day and night sides is mainly determined by variations in UV radiation, and corresponding changes in ozone lifetime, and the tidal locking of the planet results increases the inhomogeneity of ozone. Both studies also find that transported HO_x species are an important sink of night side ozone and the developing of a night side temperature inversion. However, there are some key differences in ozone (compare their Figure 3 and our Figure 2) that shows our ozone layer is much thinner than theirs, with our layer thinning rapidly above 30 km while theirs extends above 48 km. It is also unclear if their experiment results in the cold trap ozone accumulation, which is a prominent night side feature. These differences are likely due to the stellar spectral energy distributions used and the role of continental orography affecting the atmospheric dynamics.

A growing body of work has promoted the use of ozone as a potential biosignature (Schwieterman et al. (2018) and references therein). In our work we have shown that atmospheric ozone concentrations on a tidally locked planet exhibit significant spatial variations across the dayside hemisphere and between the dayside and nightside hemispheres. This illustrates the need to model planetary atmospheres in 3-D to more accurately reproduce atmospheric limb or disk-averaged spectral measurements. The rapid ozone spatial variations we show at the terminators, in particular, are relevant to transmission spectroscopy along the atmospheric limb. A similar-sized planet in a different orbit around a star, e.g. 3:2 resonance orbit, may very well also exhibit strong temporal variations in ozone, reinforcing the need to a) use 3-D models to describe ozone and other reactive chemistry and b) observe the same objects repeatedly. We anticipate a more realistic 3-D distribution of atmospheric constituents will help reduce the probability of false positives and false negatives.

Our study has brought together researchers from Earth sciences and astrophysics to improve understanding of exoplanetary atmospheres. We have used a world-leading Earth system model that has been generalized for exoplanets, providing us with a flexible numerical and scientific framework on which to develop the physical, chemical, and potentially biological processes necessary to understand the habitability of individual exoplanets within the context of observational constraints. Our work here has focused on the Chapman ozone mechanism and a catalytic cycle associated with water vapour. Competing catalytic cycles operate in Earth's atmosphere, some of which are relevant to exoplanets. The nitrogen oxide catalytic cycle, initiated through emission of NO_x (biogenically or through geological processes) or the thermal decomposition of N_2, can also lead to efficient destruction of ozone. Lightning is one such process that could achieve the necessary temperatures for thermal decomposition. More generally, processes associated with a charged atmosphere can significantly impact the physical and chemical state of the neutral atmosphere.

More broadly, we have shown that including a realistic description of radiatively active atmospheric gases that is consistent with the physical system significantly alters the physical state. Changing atmospheric heating rates via absorption of incoming and outgoing radiation alters a planet's ability to maintain liquid water at the surface and therefore being considered habitable

from an anthropic perspective. Similarly, atmospheric particles lofted by aeolian processes or from the condensation of non-volatile gases can scatter and absorb incoming and outgoing radiation. To understand the habitability of exoplanets, we have to understand their atmospheric composition that can only be achieved through self-consistent global 3-D models of atmospheric physics and chemistry.

REFERENCES

Anglada-Escudé G., et al., 2016, Nature, 536, 437

Bochanski J. J., Hawley S. L., Covey K. R., West A. A., Reid I. N., Golimowski D. A., Ivezic Z., 2010, The Astrophysical Journal, pp 2679–2699

Borucki W. J., 2016, Reports on Progress in Physics, 79, 036901

Boutle I. A., Mayne N. J., Drummond B., Manners J., Goyal J., Hugo Lambert F., Acreman D. M., Earnshaw P. D., 2017, Astronomy & Astrophysics, 601, A120

Chapman S., 1930, Memoirs of the Royal Meteorological Society

Charbonneau D., Brown T. M., Noyes R. W., Gilliland R. L., 2002, The Astrophysical Journal, 568, 377

Chen H., Wolf E. T., Kopparapu R., Domagal-Goldman S., Horton D. E., 2018, The Astrophysical Journal, 868, L6

Drummond B., et al., 2018, The Astrophysical Journal, 855, L31

Edwards J. M., Slingo A., 1996, Quarterly Journal of the Royal Meteorological Society, 122, 689

Ganzeveld L., Lelieveld J., 1995, Journal of Geophysical Research: Atmospheres, 100, 20999

Giannakopoulos C., Chipperfield M. P., Law K. S., Pyle J. A., 1999, Journal of Geophysical Research: Atmospheres, 104, 23761

Gillon M., et al., 2017, Nature, 542, 456

Kasting J. F., 1988, Icarus, 74, 472

Kasting J. F., Whitmire D. P., Reynolds R. T., 1993, Icarus, 101, 108

Kopparapu R. K., Wolf E. T., Arney G., Batalha N. E., Haqq-Misra J., Grimm S. L., Heng K., 2017, The Astrophysical Journal, 845, 5

Lagrange A.-M., et al., 2010, Science, 329, 57

Léger, A. et al., 2009, A&A, 506, 287

Lewis N. T., Lambert F. H., Boutle I. A., Mayne N. J., Manners J., Acreman D. M., 2018, The Astrophysical Journal, 854, 171

Mann G. W., Carslaw K. S., Spracklen D. V., Ridley D. A., Manktelow P. T., Chipperfield M. P., Pickering S. J., Johnson C. E., 2010, Geoscientific Model Development, 3, 519

Manners J., Edwards J. M., Hill P., Thelen J.-C., 2015, Technical report, SOCRATES (Suite Of Community RAdiative Transfer codes based on Edwards and Slingo) Technical Guide. Met Office, UK

Mayne N. J., Baraffe I., Acreman D. M., Smith C., Wood N., Amundsen D. S., Thuburn J., Jackson D. R., 2014a, Geoscientific Model Development, 7, 3059

Mayne N. J., et al., 2014b, Astronomy and Astrophysics, 561, 1

Mayor M., Queloz D., 1995, A Jupiter-mass companion to a solar-type star, doi:10.1038/378355a0

Meadows V. S., Barnes R. K., 2018, in , Handbook of Exoplanets. Springer International Publishing, Cham, pp 1–24, doi:10.1007/978-3-319-30648-3_57-1, http://link.springer.com/10.1007/978-3-319-30648-3_57-1

Meadows V. S., et al., 2018, Astrobiology, 18, 133

Morgenstern O., et al., 2013, Journal of Geophysical Research: Atmospheres, 118, 1028

Morton T. D., Bryson S. T., Coughlin J. L., Rowe J. F., Ravichandran G., Petigura E. A., Haas M. R., Batalha N. M., 2016, The Astrophysical Journal, 822, 1

O'Malley-James J. T., Kaltenegger L., 2017, Monthly Notices of the Royal Astronomical Society: Letters, 469, L26

Palmer T. N., 2012, Quarterly Journal of the Royal Meteorological Society, 138, 841

Proedrou E., Hocke K., 2016, Earth, Planets and Space, 68, 96

Quintana E. V., et al., 2014, Science, 344, 277

Rajpurohit A. S., Reylé C., Allard F., Homeier D., Schultheis M., Bessell M. S., Robin A. C., 2013, Astronomy & Astrophysics, 556, A15

Roney P., 1965, Journal of Atmospheric and Terrestrial Physics, 27, 1177

Schwieterman E. W., et al., 2018, Astrobiology, 18, 663

Seager S., 2014, Proceedings of the National Academy of Sciences, 111, 12634

Seager S., Kuchner M., Hier-Majumder C. A., Militzer B., 2007, The Astrophysical Journal, 669, 1279

Segura A., Walkowicz L. M., Meadows V., Kasting J., Hawley S., 2010, Astrobiology, 10, 751

Shields A. L., Meadows V. S., Bitz C. M., Pierrehumbert R. T., Joshi M. M., Robinson T. D., 2013, Astrobiology, 13, 715

Shields A. L., Ballard S., Johnson J. A., 2016, Physics Reports, 663, 1

Showman A. P., Polvani L. M., 2011, The Astrophysical Journal, 738, 71

Sing D. K., et al., 2011, A&A, 527, A73

Spiegel D. S., Fortney J. J., Sotin C., 2014, Proceedings of the National Academy of Sciences, 111, 12622

Telford P. J., et al., 2013, Geoscientific Model Development, 6, 161

Thompson S. E., et al., 2018, The Astrophysical Journal Supplement Series, 235, 38

Tilley M. A., Segura A., Meadows V., Hawley S., Davenport J., 2019, Astrobiology

Todorov K. O., Deming D., Burrows A., Grillmair C. J., 2014, The Astrophysical Journal, 796, 100

Tompkins A. M., 2000, Monthly Weather Review, 128, 1521

Turbet M., Forget F., Head J. W., Wordsworth R., 2017, Icarus, 288, 10

Walker J. C. G., Hays P. B., Kasting J. F., 1981, Journal of Geophysical Research: Oceans, 86, 9776

Walters D., et al., 2017, Geoscientific Model Development Discussions, 2017, 1

Weiss L. M., Marcy G. W., 2014, The Astrophysical Journal, 783, L6

Wild O., Zhu X., Prather M. J., 2000, Journal of Atmospheric Chemistry, 37, 245

Yang J., Abbot D. S., 2014, The Astrophysical Journal, 784, 155

APPENDIX A: PHYSICAL DESCRIPTION OF NUMERICAL EXPERIMENTS

Here, we focus on the meteorological variables that complement the ozone chemistry fields shown in the main paper.

Figure A1 shows that surface temperatures on a significant portion of the dayside hemisphere are warmer than the 273 K triple point. Our calculations show that the planet can sustain liquid water at the planetary surface (Boutle et al. 2017). On the nightside there are symmetrically-placed cold traps at ±50° latitude in the northern and southern hemispheres, where temperatures are ≃150 K. Both cold traps are associated with cyclonic movement. After the cold trap, air masses move towards polar latitudes before rejoining the atmospheric jets at the anti-stellar point, where there is a reversal in the meridional wind direction at approximately at a longitude of 225° (Figures A2 and A3). These cold traps result in longer, localized residence times for air that impacts ozone chemistry (not shown). These meteorological features are described further by Showman & Polvani (2011).

Maintenance of an atmospheric jet at 30 km (Figure A2) provides a mechanism to warm the equatorial band on the nightside, where atmospheric temperatures still remain below 273 K. We find a second jet structure on the nightside below 10 km, with zonal winds peaking close to the anti-stellar point (longitude 225°). Between the jet streams on the day and night sides of the planet we find layers where the wind speed is very low. Wind speeds in the meridional direction (Figure A3), driven by the Coriolis force due to the planet orbiting its host star, are much slower than zonal wind speeds that are driven by the thermal gradient between the day and night sides. We also find a persistent thermal inversion on the nightside with air between 2 and 5 km warmer than at the surface. The maximum and minimum mean temperatures on the planet are 287 K and 147 K, respectively. These mean extreme values are ≃3 K cooler than values consistent with Earth-like ozone distributions (Boutle et al. 2017).

Figure A4 shows the distribution of UV radiation as it passes through the atmosphere. UV is non-zero on the dayside, as expected, with smaller values towards the terminators. It is relatively constant throughout the atmosphere, with a shallow gradient below 30 km, due to ozone photolysis, followed by a sharp drop below 10 km due to cloud reflectivity that peaks at the substellar point. This is similar to what happens on Earth. High-energy UVC is rapidly absorbed at high altitudes, UVB is absorbed more slowly as it passes through the stratospheric ozone layer, and UVA is attenuated at lower altitudes but can also reach the surface. Our surface UV levels are approximately 100 times lower than values we find on a similar planet with an Earth-like top-of-the-atmospheric radiation flux using the same planetary configuration but using a Sun-like spectral energy distribution, a star-planet orbit of 1 AU, and a day length of 24 hrs. This weaker level of incoming stellar UV radiation is still sufficiently energetic to establish and maintain an atmosphere ozone layer.

APPENDIX B: ADDITIONAL 3-D CHEMISTRY FIELDS

Figures B1 and B2 describe the key reaction fluxes associated with the HO_x catalytic cycle (reactions R5-R8 from the main text). Figures B3 and B4 describe the atmospheric lifetime and atmospheric residence time due to chemical and transport processes, respectively.

This paper has been typeset from a TeX/LaTeX file prepared by the author.
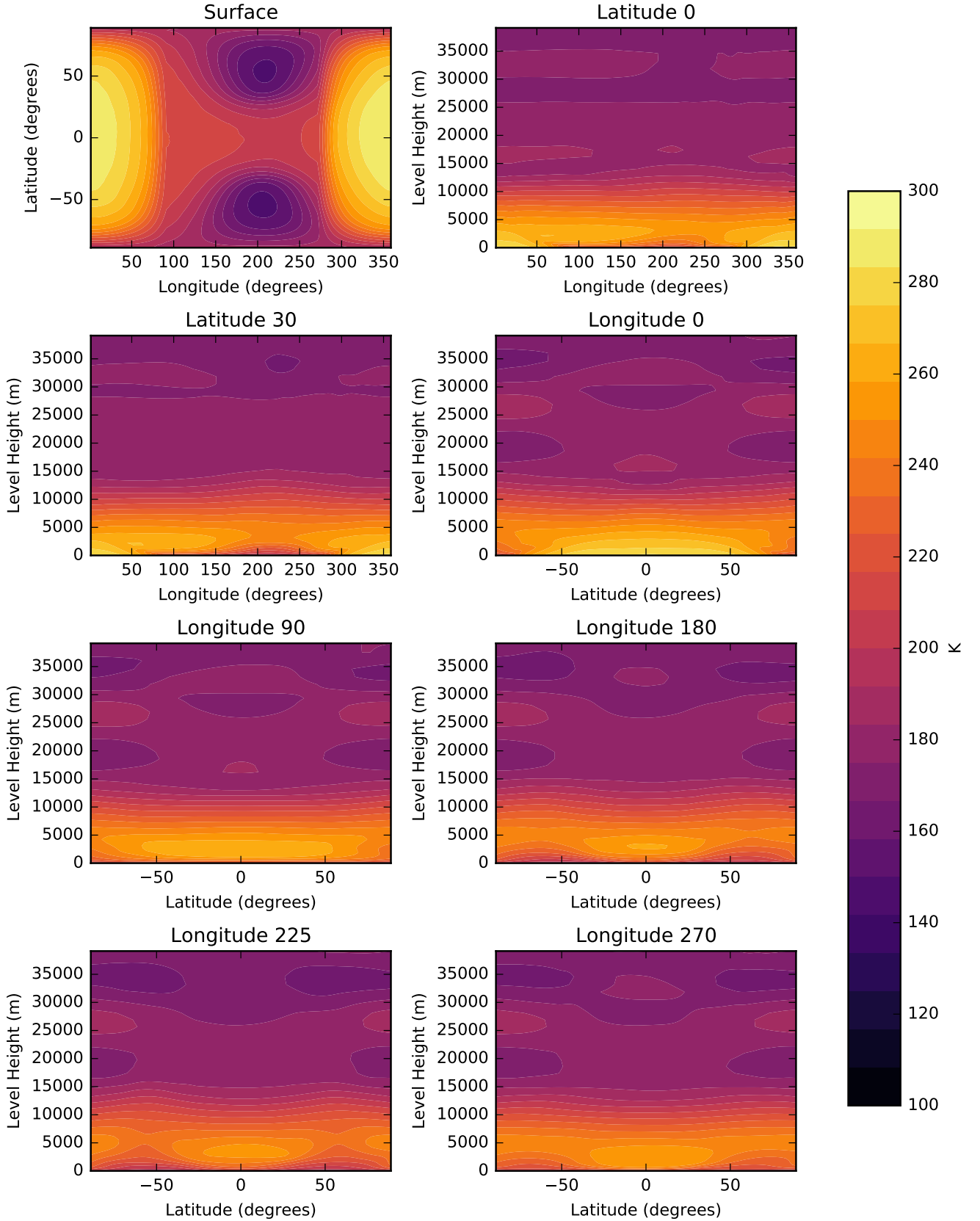
Figure A1. Air temperature in the simulated atmosphere. Panels show means over 120 days of model time. The top left panel shows surface temperature. Remaining panels show slices through latitudes 0°, 30° and longitudes 0°, 90°, 180°, 225° and 270°.
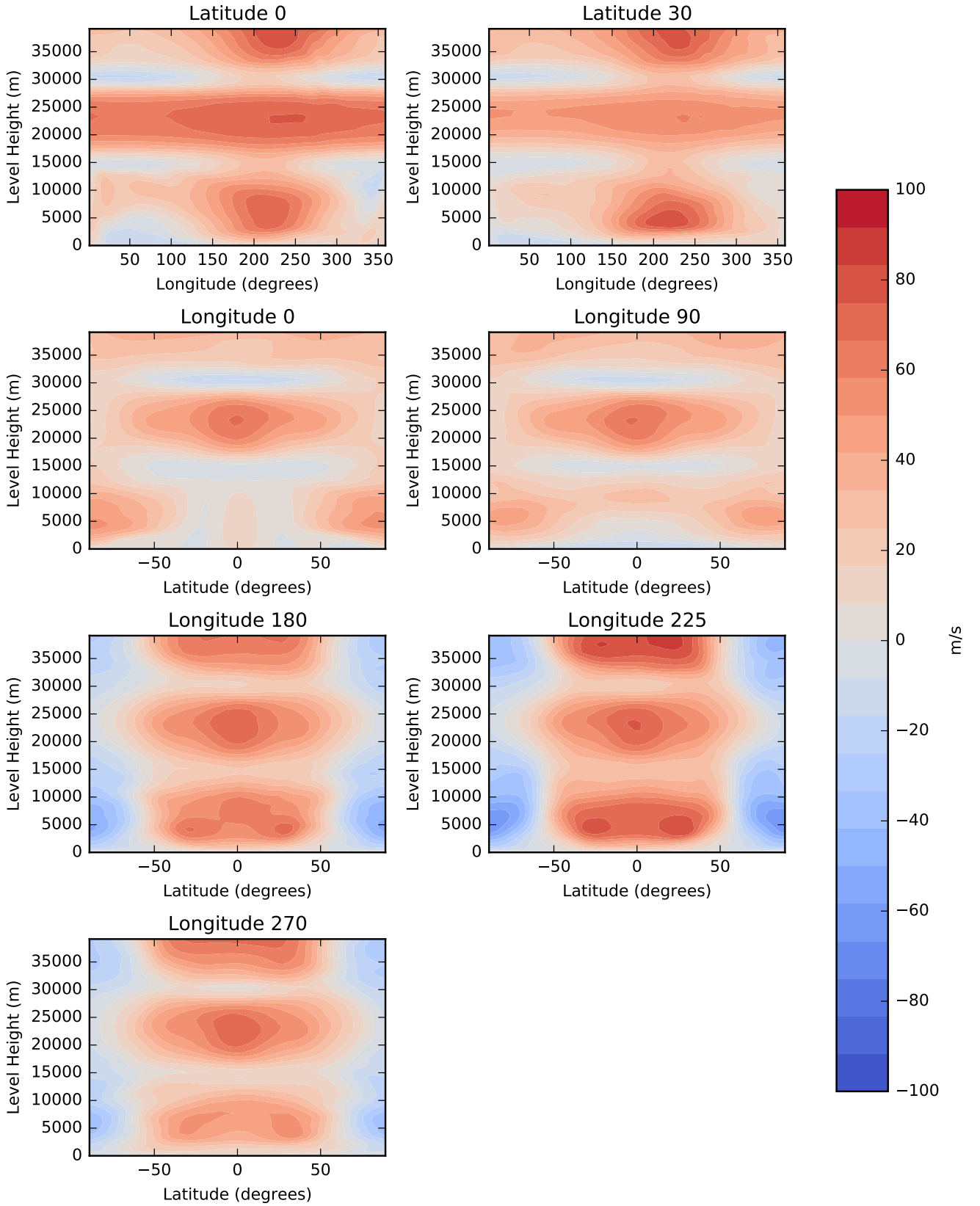
Figure A2. Zonal winds in the simulated atmosphere. Panels show means over 120 days of model time. Panels show slices through latitudes 0°, 30° and longitudes 0°, 90°, 180°, 225° and 270°.
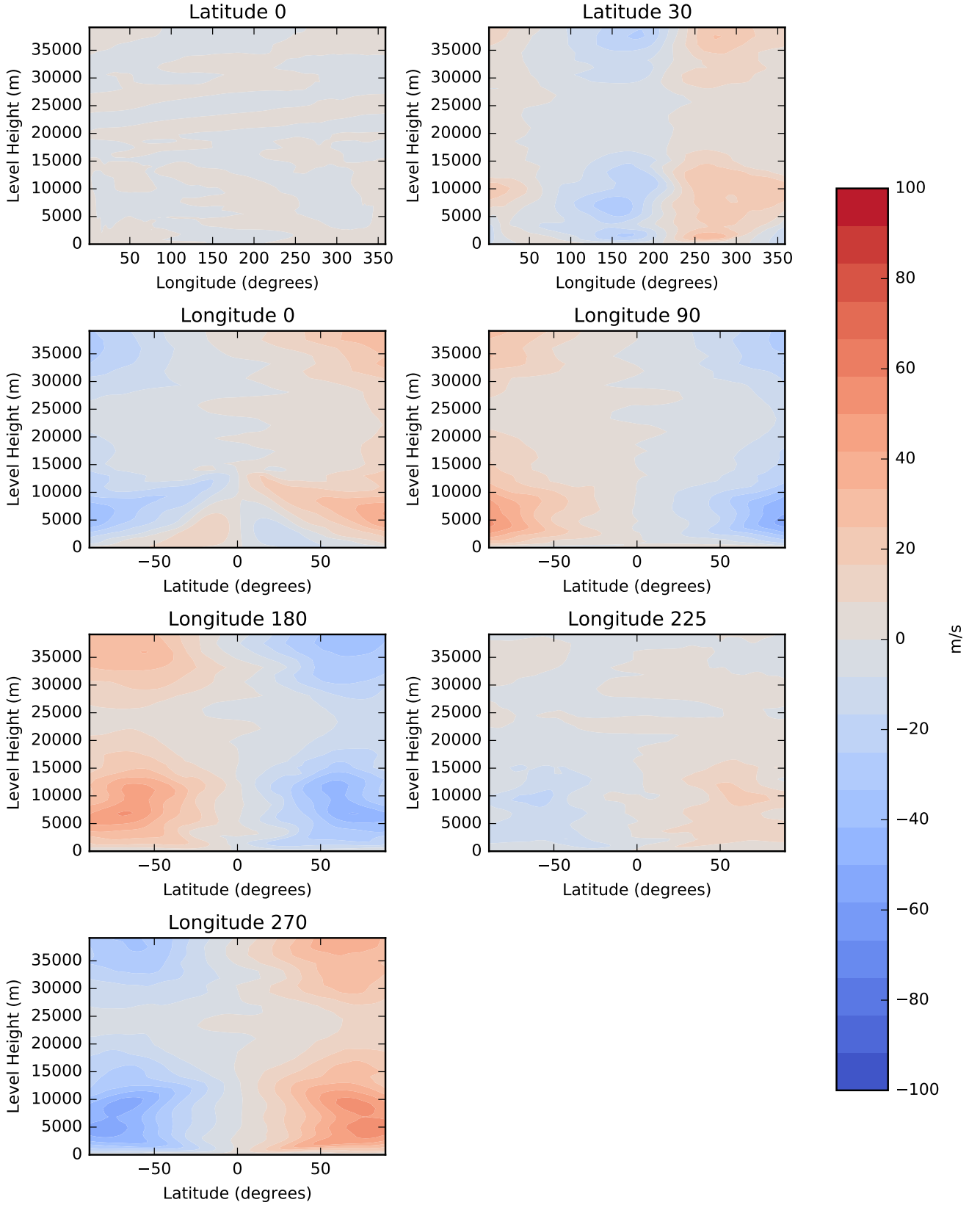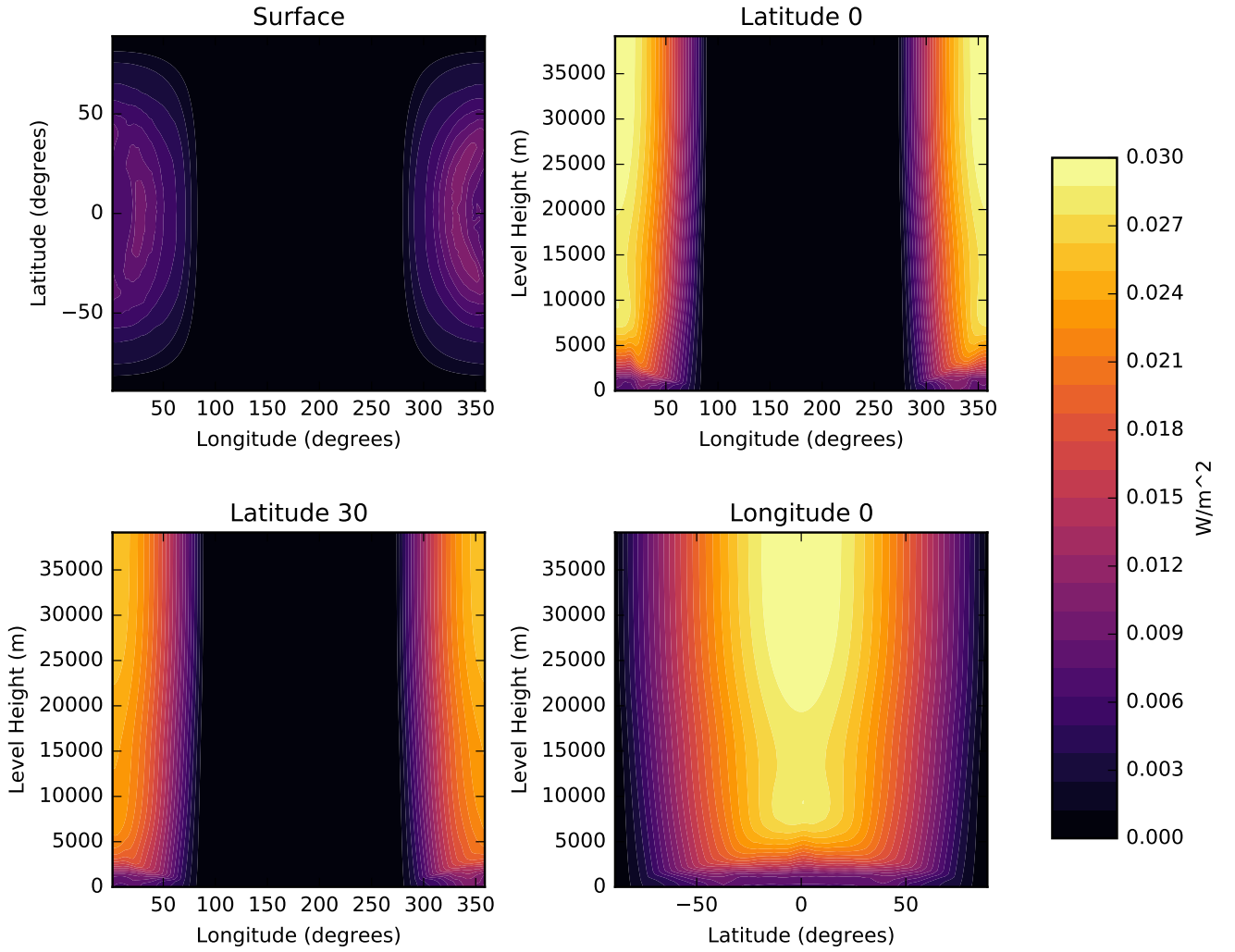
Figure A3. Meridional winds in the simulated atmosphere. Panels show means over 120 days of model time. Panels show slices through latitudes 0°, 30° and longitudes 0°, 90°, 180°, 225° and 270°.

Figure A4. Downward UV in the simulated atmosphere. Panels show means over 120 days of model time. The top left panel shows surface UV. Remaining panels show slices through latitudes 0°, 30° and longitudes 0°. We do not show the nightside plots here as there is obviously no UV flux at these locations.
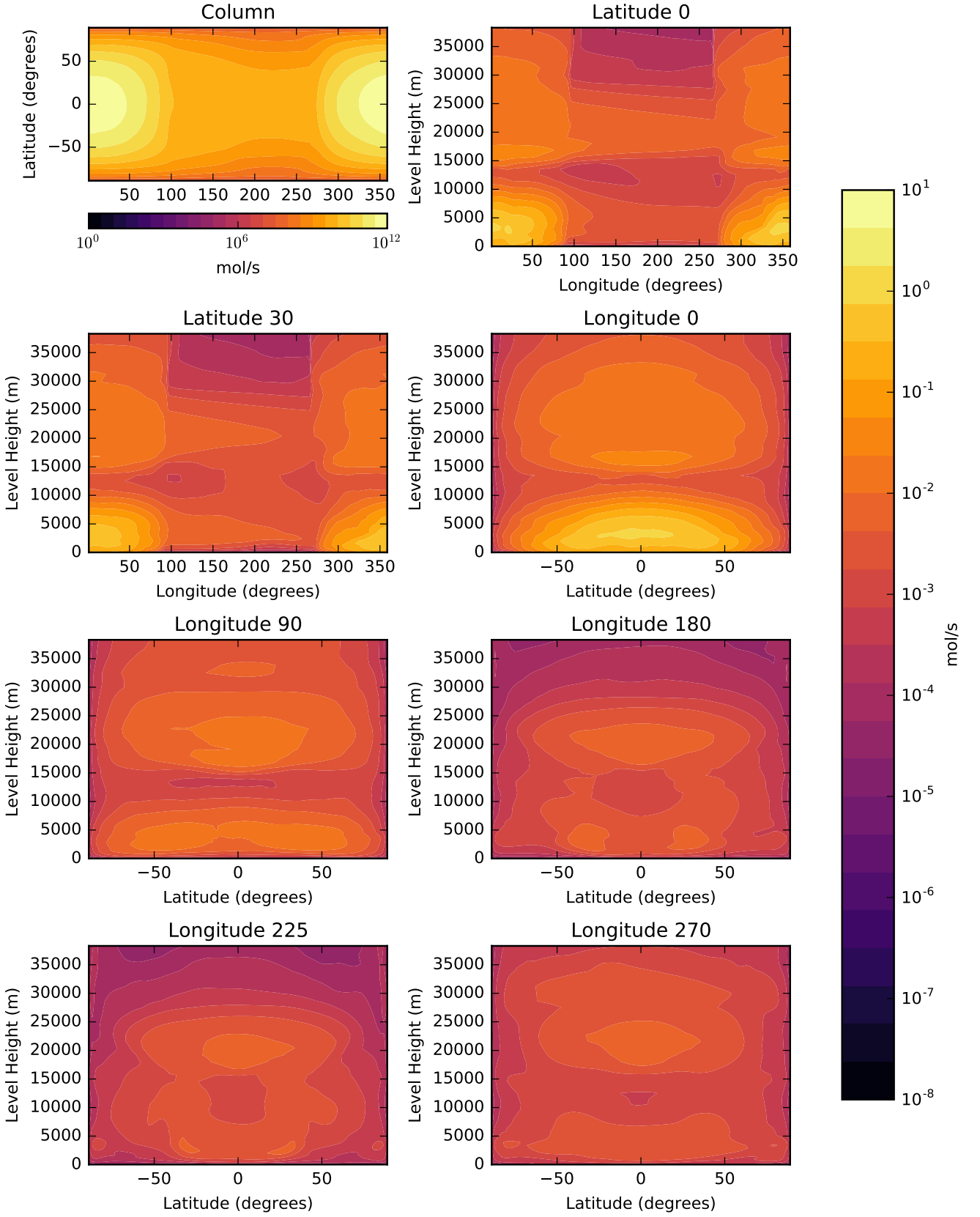
Figure B1. As Figure 5 but for reaction flux (mol/s) OH+O$_3$→HO$_2$+O$_2$ (reaction R6).
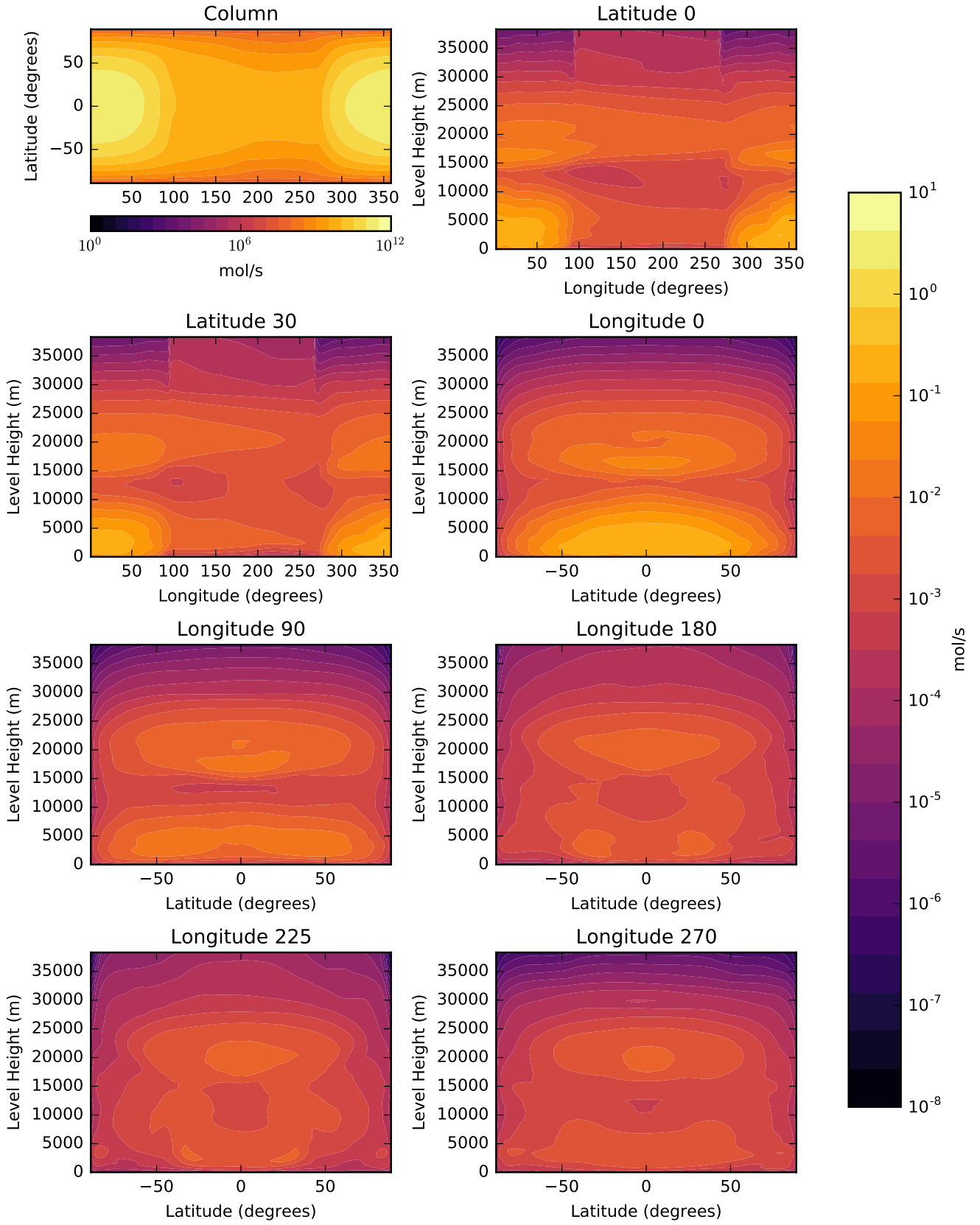
Figure B2. As Figure 5 but for reaction flux (mol/s) HO$_2$+O$_3$→OH+2O$_2$ (reaction R7).
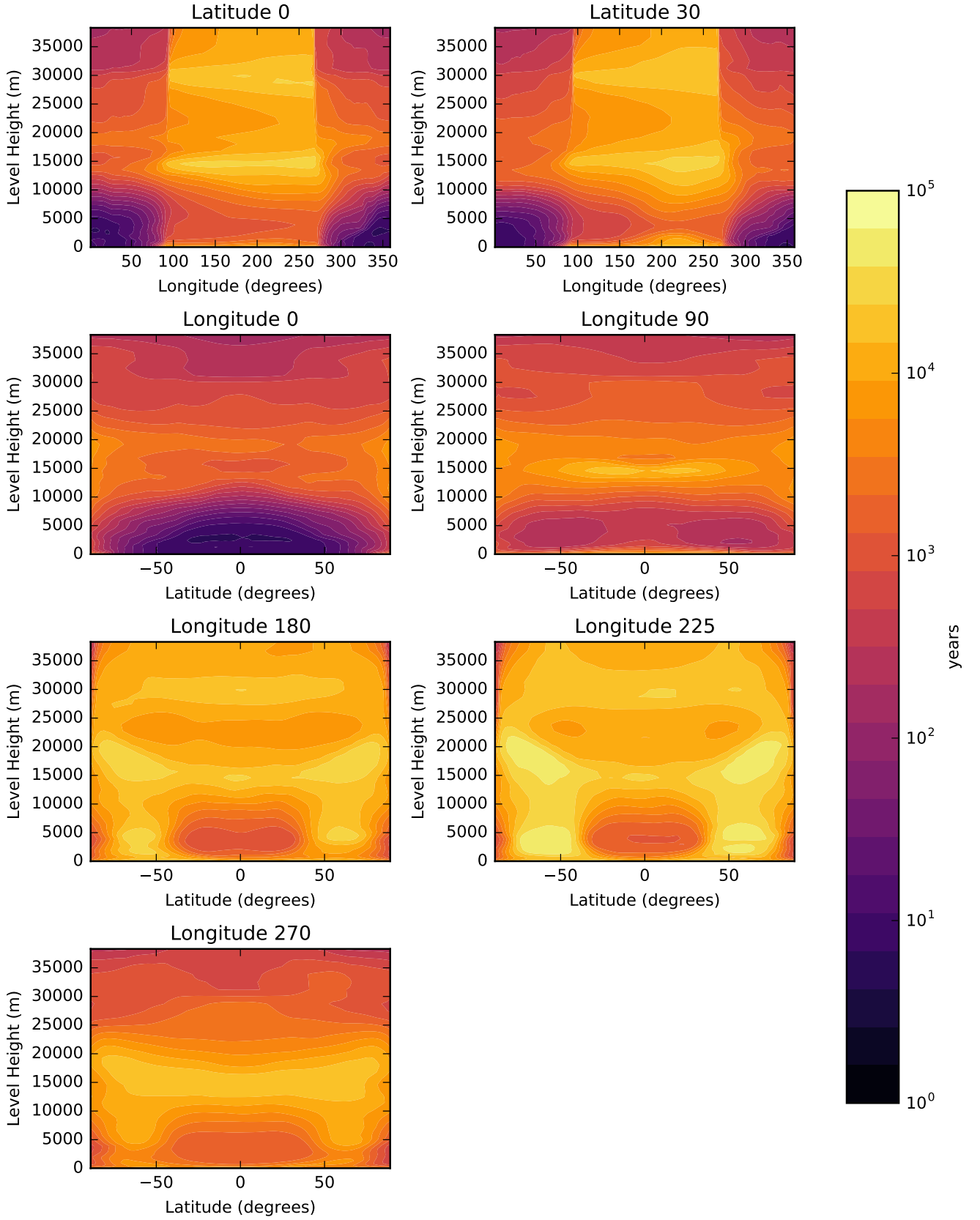
Figure B3. Net O_3 lifetime. Panels show means over 120 days of model time. Panels show slices through latitudes 0°, 30° and longitudes 0°, 90°, 180°, 225° and 270°.
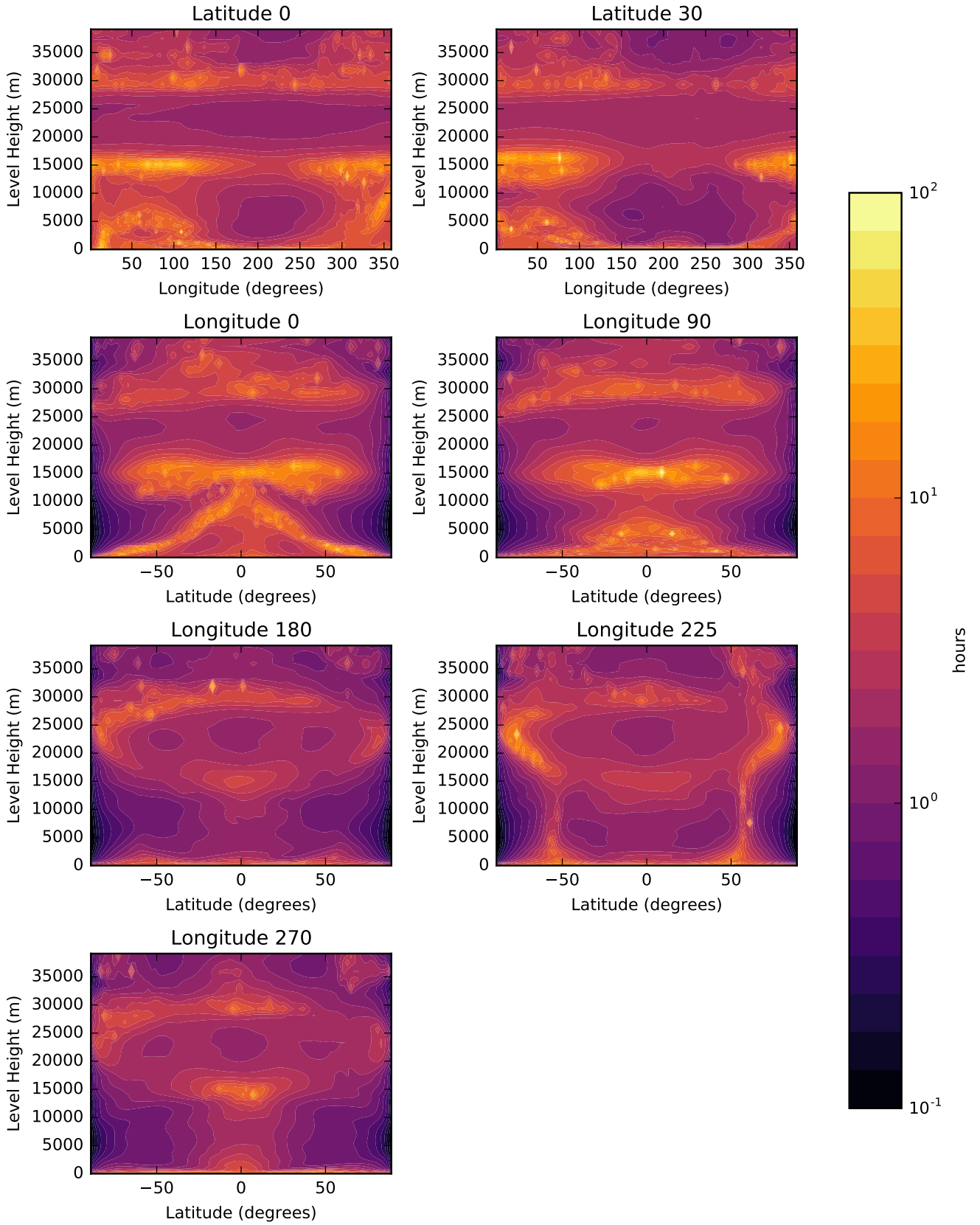
Figure B4. Transport residence time for each grid box in the atmosphere. Panels show means over 120 days of model time. Panels show slices through latitudes 0°, 30° and longitudes 0°, 90°, 180°, 225° and 270°.